Experimental Neurology 347 (2022) 113900

Contents lists available at ScienceDirect

Experimental Neurology

journal homepage: www.elsevier.com/locate/yexnr

Research paper

Rab7 reduces α-synuclein toxicity in rats and primary neurons

Eva M. Szegö [a], Chris Van den Haute [b,c], Lennart Höfs [a], Veerle Baekelandt [b,c], Anke Van der Perren [b,1], Björn H. Falkenburger [a,d,e,f,1,*]

[a] Department of Neurology, TU Dresden, Dresden, Germany
[b] Laboratory for Neurobiology and Gene Therapy, Department of Neurosciences, Leuven Brain Institute, KU Leuven, Leuven, Belgium
[c] Leuven Viral Vector Core, KU Leuven, Leuven, Belgium
[d] Deutsches Zentrum für Neurodegenerative Erkrankungen, Dresden, Germany
[e] Department of Neurology, RWTH Aachen University, Aachen, Germany
[f] JARA-BRAIN Institute Molecular Neuroscience and Neuroimaging, Forschungszentrum Jülich GmbH and RWTH Aachen University, Aachen, Germany

ARTICLE INFO

Keywords:
alpha-Synuclein
Rab7
Protein aggregation
Parkinson's disease
DNA damage
Oxidative stress
Autophagy
Neuroprotection

ABSTRACT

During the pathogenesis of Parkinson's disease (PD), aggregation of alpha-synuclein (αSyn) induces a vicious cycle of cellular impairments that lead to neurodegeneration. Consequently, removing toxic αSyn aggregates constitutes a plausible strategy against PD. In this work, we tested whether stimulating the autolysosomal degradation of αSyn aggregates through the Ras-related in brain 7 (Rab7) pathway can reverse αSyn-induced cellular impairment and prevent neurodegeneration in vivo. The disease-related A53T mutant of αSyn was expressed in primary neurons and in dopaminergic neurons of the rat brain simultaneously with wild type (WT) Rab7 or the T22N mutant as negative control. The cellular integrity was quantified by morphological and biochemical analyses. In primary neurons, WT Rab7 rescued the αSyn-induced loss of neurons and neurites. Furthermore, Rab7 decreased the amount of reactive oxygen species and the amount of Triton X-100 insoluble αSyn. In rat brain, WT Rab7 reduced αSyn-induced loss of dopaminergic axon terminals in the striatum and the loss of dopaminergic dendrites in the substantia nigra pars reticulata. Further, WT Rab7 lowered αSyn pathology as quantified by phosphorylated αSyn staining. Finally, WT Rab7 attenuated αSyn-induced DNA damage in primary neurons and rat brain. In brief, Rab7 reduced αSyn-induced pathology, ameliorated αSyn-induced neuronal degeneration, oxidative stress and DNA damage. These findings indicate that Rab7 is able to disrupt the vicious cycle of cellular impairment, αSyn pathology and neurodegeneration present in PD. Stimulation of Rab7 and the autolysosomal degradation pathway could therefore constitute a beneficial strategy for PD.

List of abbreviations

53BP1	tumor suppressor p53-binding protein 1
DAB	3,3-diaminobenzidine
DAT	dopamine transporter
DCFH-DA	dichlorodihydrofluorescein diacetate
DIV	days in vitro
DLB	dementia with Lewy bodies
GC	genome copy
GFP	green fluorescent protein
JC-1	tetraethylbenzimidazolylcarbocyanine iodide
LDH	lactate dehydrogenase
LN	Lewy neurites
MSA	multiple system atrophy
PD	Parkinson's disease
phospho-αSyn	phosphorylated alpha-synuclein
PSD95	postsynaptic density protein 95
rAAV	recombinant adeno-associated viral vector
Rab7	Ras-related in brain 7
ROS	reactive oxygen species
SN	substantia nigra
SNc	substantia nigra pars compacta
SNr	substantia nigra pars reticulata
TBS	Tris-buffered saline
TH	tyrosine hydroxylase

(*continued on next column*)

(*continued*)

(*continued on next page*)

* Corresponding author at: Department of Neurology, Technische Universität Dresden, Fetscherstraße 74, 01307 Dresden, Germany.
E-mail addresses: Eva.Szego@uniklinikum-dresden.de (E.M. Szegö), chris.vandenhaute@kuleuven.be (C. Van den Haute), lennart.hoefs@rwth-aachen.de (L. Höfs), veerle.baekelandt@kuleuven.be (V. Baekelandt), anke.vanderperren@kuleuven.be (A. Van der Perren), bfalken@ukdd.de (B.H. Falkenburger).
[1] AVdP and BHF contributed equally to this work.

https://doi.org/10.1016/j.expneurol.2021.113900
Received 12 July 2021; Received in revised form 19 September 2021; Accepted 18 October 2021
Available online 22 October 2021

(*continued*)

VMAT2	vesicular monoamine transporter 2
WT	wild type
αSyn	alpha-synuclein

1. Introduction

Aggregation and accumulation of alpha-synuclein (αSyn) are key events in Parkinson's disease (PD) and other synucleinopathies. αSyn monomers are mainly located at presynaptic vesicles whereas misfolded αSyn oligomers and high molecular weight species can be found throughout the entire neuron. αSyn pathology affects diverse cellular functions, including: increasing reactive oxygen species (ROS), impaired mitochondrial function (Junn and Mouradian, 2002; Szegő et al., 2019), reduced proteasomal degradation and autophagy (Suzuki et al., 2020; Winslow and Rubinsztein, 2011) as well as DNA damage (Wang et al., 2016b). However, the pathogenesis of PD does not follow a linear succession of events and is rather characterized by self-enhancing mechanisms. ROS and impaired mitochondrial function also increase αSyn pathology (Goodwin et al., 2013; Scudamore and Ciossek, 2018), as does impaired protein quality control and clearance (Klucken et al., 2012; Minakaki et al., 2018; Winslow and Rubinsztein, 2011). Moreover, autophagy can protect against oxidative stress (Galati et al., 2019; Guo et al., 2013; Kiffin et al., 2006) while oxidative stress can impair autophagy (Burgoyne, 2018; Frudd et al., 2018). DNA damage can also result from ROS imbalance (Milanese et al., 2018; Paiva et al., 2017), and it can induce autophagy (Eapen et al., 2017). Taken together, toxic αSyn species initiate a vicious circle of protein aggregation and cellular dysfunction. Removing toxic αSyn species has the potential to disrupt this toxic feedback loop, improve neuronal health and slow disease progression in synucleinopathies.

Aggregated αSyn is degraded via the autophago-lysosomal pathway. Mutations in genes encoding autophago-lysosomal pathway proteins, such as glucocerebrosidase (GBA), ATPase cation transporting 13A2 (ATP13A2), Ras-related in brain 39B (Rab39B), ADP-ribosylation factor-like protein 8B (Arl8b), lysine acetyltransferase 8 (KAT8), Ras-related in brain guanine nucleotide exchange factor 1 (RabGEF1) or vacuolar protein sorting ortholog 35 (VPS35), cause impairment of degradation, and are risk factors for PD (Bandres-Ciga et al., 2019; Chang et al., 2017; Gao et al., 2018; Sidransky et al., 2009; Verstraeten et al., 2015). The multi-step process of autophagy is regulated by several critical proteins, including the Ras-related in brain (Rab) family of small GTPases. Ras-related in brain 7 (Rab7) orchestrates trafficking of autophagosomes and late endosomes, catalyzes the fusion of autophagosomes with lysosomes, and regulates late maturation of autophagosomes. Rab7 malfunction hampers autolysosome formation, leads to the accumulation of dysfunctional autophagosomes and consequently impairs protein degradation (Baba et al., 2019; Kjos et al., 2017; Kuchitsu and Fukuda, 2018; Zhan et al., 2017). We previously demonstrated that Rab7 is the rate-limiting factor for αSyn aggregate clearance; its overexpression facilitates the removal of αSyn inclusions in human cells and alleviates αSyn-induced motor phenotype in fruit flies (Dinter et al., 2016).

In the present work, we investigated whether mammalian neurons can be protected against αSyn toxicity by Rab7-induced stimulation of aggregate clearance. Expression of αSyn carrying the disease-related A53T mutation was achieved in mouse primary neurons and in dopaminergic neurons of rat substantia nigra (SN) by a recombinant adeno-associated viral vector 2/7 (rAAV) as previously described (Karpinar et al., 2009; Van der Perren et al., 2015; Van Der Perren et al., 2011). Wild-type (WT) Rab7 was also expressed using rAAV. As a negative control, we used the Rab7 mutant T22N, which binds Rab7 effectors but not guanosine-5′-triphosphate (GTP) (Spinosa et al., 2008). First, we assessed the effect of Rab7 on αSyn pathology, αSyn-induced DNA damage, oxidative stress and cell death in mouse primary neurons. Second, we analyzed the integrity of the dopaminergic nigrostriatal neurons in vivo. Finally, we investigated αSyn accumulation and DNA damage in the dopaminergic neurons. We demonstrate that inducing Rab7-mediated clearance of αSyn aggregates in neurons improves cellular integrity and reduces neurodegeneration.

2. Materials and methods

Source of chemicals, antibodies, composition of buffers, equipment and software used in this study are listed in Supplemental Table S1.

2.1. Recombinant AAV production and purification

Vector production and purification was carried out as previously described (Van Der Perren et al., 2011). The plasmids include: the constructs for the AAV7 serotype, the AAV transfer plasmid encoding either the human A53T mutant αSyn, the enhanced green fluorescent protein (GFP), human WT Rab7 with a double N-terminal HA-tag or T22N Rab7 with a double N-terminal HA-tag, under the control of the CMVie enhanced synapsin1 promoter and the pAdvDeltaF6 adenoviral helper plasmid. Real-time PCR analysis was used for genomic copy (GC) determination.

2.2. Primary neuronal culture

Primary cortical cultures were prepared from P1-3 C57BL6/J mouse pups of mixed sex as previously described (Szegő et al., 2019). Briefly, after dissection and trypsination, dissociated neurons were plated onto poly-L-ornithine coated glass coverslip (100,000 cells per well in 24-well dishes), and maintained in Neurobasal A medium containing 2% B27, 0.5 mM glutamax and antibiotics. One third of the medium was changed on every third day, and from the second medium change on, no antibiotics were added. On DIV 12, neurons were transduced with one of the following combinations of rAAV vectors: (1) GFP, (2) GFP with T22N Rab7A, (3) GFP with WT Rab7A, (4) A53T αSyn with GFP, (5) A53T αSyn with T22N Rab7A or (6) A53T αSyn with WT Rab7A (final concentration for all 1.0e+9 GC/ml). Cells were fixed (4% paraformaldehyde, 10 min, 20 °C) on DIV 15 for phospho-αSyn and LAMP1, and for PSD95 and MAP2 labeling. Cells were fixed on DIV 16 for detecting 53BP1. Cells were fixed or lysed on DIV 18 or DIV 20 for toxicity and comet assays.

2.3. Microfluidic chambers for axonal regeneration assay

The effect of WT and T22N Rab7 on αSyn-induced inhibition of axonal regeneration was measured as previously described (Park et al., 2006). Primary cortical neurons were seeded in silicone microfluidic devices with 450 μm groove length according to the manufacturer's protocol. After bonding the microfluidic devices to a glass coverslip precoated with poly-L-ornithine, 100,000 cells (5.0e+6/ml) were plated in the cell compartment. The axonal side of the chamber was filled with 200 μl complete Neurobasal medium. After attachment of the cells, 200 μl medium was added in the cell compartment as well. One third of the medium was changed every third day on both sides. On DIV 12, neurons were infected with rAAV (final concentration for all 5e+8 GC/ml). On DIV 15, axons were mechanically cut by an air bubble. Cells were fixed on DIV 20 and stained for tubulin (PRB—435P, followed by Alexa 555-labeled anti-mouse secondary antibody). Axonal length in the distal compartment was measured using ImageJ by drawing a segmented line along each individual axon projecting out of the microgroove.

2.4. Animals and surgery

All animal experiments were carried out in accordance with the European Communities Council Directive of November 24, 1986 (86/

609/EEC) and approved by the Bioethical Committee of the KU Leuven (ECD project P067-2013 and P085-2014, Belgium). Eight-week-old female Wistar rats (Janvier, France, 200–250 g) were housed under a 12-h light and/or dark cycle with free access to pelleted food and tap water. All surgical procedures were performed using aseptic techniques. Rats were anaesthetized with ketamine (60 mg/kg, intraperitoneal (i.p.), Ketalar, Pfizer, Belgium) and medetomidine (0.4 mg/kg, i.p., Dormitor, Pfizer). 3 μl of vector mix containing the rAAV A53T αSyn vector (9.0E11 GC/ml, injected genome copies 1,35E9) and rAAV HA-Rab7A T22N vector (9,3E11 GC/ml, injected genome copies 1,39E9) or the rAAV HA-Rab7A WT vector (9,3E11 GC/ml, injected genome copies 1,39E9) was injected in the substantia nigra (AP: −5.3; L: −2.0; DV: −7.2 from dura, using Bregma as reference) with a Hamilton syringe (Hamilton, Bonaduz, GR, Switzerland) as previously described (Van der Perren et al., 2015, 2016).

Forelimb use was quantified by the cylinder test four weeks after the unilateral rAAV-injection. Contacts made by each forepaw with the wall of a 20-cm-wide clear glass cylinder were scored from the videotapes by an observer blinded to the animal's identity. A total of 25 contacts were recorded for each animal, and the impaired (left) forelimb usage was expressed as a percentage of total forelimb contacts. Non-lesioned control rats score around 50% in this test.

Rats were sacrificed four weeks after the rAAV-injection with an overdose of sodium pentobarbital (200 mg/kg, i.p.) followed by intracardial perfusion with 4% paraformaldehyde in PBS. After post-fixation (4% paraformaldehyde, overnight), 50 μm-thick coronal brain sections were cut with a vibrating microtome.

2.5. Immunohistochemical and immunofluorescent stainings

To quantify the number of dopaminergic neurons in the substantia nigra (SN) and the density of dopaminergic axon terminals (fibers) in the striatum, free-floating sections were stained for tyrosine hydroxylase (TH, Ab152). αSyn pathology was quantified after staining for αSyn phosphorylated at Serine 129 (phospho-αSyn, 11A5). Sections were pretreated with 3% hydrogen peroxide (10 min) and incubated with primary antibody in 10% normal goat serum overnight. Incubation with biotinylated anti-rabbit IgG (TH) and anti-mouse IgG (phospho-αSyn) secondary antibodies was followed by streptavidin - horseradish peroxidase complex. TH immunoreactivity was visualized using Vector SG as a chromogen and phospho-αSyn immunoreactivity was visualized using 3,3-diaminobenzidine (DAB).

To determine neuroinflammation, every sixth striatal section was stained for the astroglia marker glial fibrillary acidic protein (GFAP, ab4674) and for the microglia marker Iba1 (019–19,741) by incubation with primary antibodies at 4 °C overnight and fluorescently labeled secondary antibodies (Alexa 488 conjugated goat anti-chicken and Alexa 555 conjugated donkey anti-rabbit, 120 min at 20 °C). Sections were counterstained with Hoechst and mounted with Fluoromount-G.

To detect DNA damage, brain slices from the SN (minimum 3 sections per animal) were stained for 53BP1 (PA5–54565), human αSyn (ALX-804-258-L001) and the HA-tag of Rab7 (MMS-101P). After incubation with secondary antibodies (Alexa 488 conjugated anti-rat, Alexa 555 conjugated anti-rabbit, and Alexa 405 conjugated anti-mouse), sections were also mounted with Fluoromount-G.

Fixed primary neurons were permeabilized using 0.2% Triton X-100 in Tris-buffered saline (TBS, pH 7.4, 10 min). Non-specific sites were blocked by 2% bovine serum albumin in TBS (RT, 1 h). The following primary antibodies were applied in blocking solution (4 °C, overnight): Microtubule-associated protein 2 (MAP2, ab5392), Lysosomal-associated membrane protein 1 (LAMP1, ab208943), 53BP1 (as above), human αSyn (as above), phosphorylated αSyn (ab51253), PSD95 (Cell Signaling, 3450) and HA-tag (as above). Secondary antibodies were: Alexa 647 conjugated anti-chicken, Alexa 555 conjugated anti-rabbit, Alexa 488 conjugated anti-rat and Alexa 405 conjugate anti-mouse. Coverslips were mounted with Fluoromount G. Co-occurance of phospho-αSyn and LAMP1 signal was determined by using the Manders` overlap coefficient (ImageJ, JACoP plugin), as fraction of phospho-αSyn signal within LAMP1 signal as previously (Dunn et al., 2011; Szegő et al., 2019). Mean fluorescent intensity of phospho-αSyn signal was measured within the MAP2 positive area as previously (Szegő et al., 2021).

2.6. Analysis of dopaminergic neurons, αSyn pathology and gliosis

The number of cells in the SN positive for TH and phospho-αSyn was determined by stereological measurements using the Optical fractionator method in a computerized system as described before (Baekelandt et al., 2002) (StereoInvestigator). Every fifth section throughout the entire SN was analyzed, 7 sections for each animal. The coefficient of error calculated according to the procedure of Schmitz and Hof (2005), varied between 0.05 and 0.10. The volume of striatal lesion was determined by quantifying the TH-positive terminals using the Cavalieri method (Stereologer). Every fifth section covering the entire extent of the striatum was included in the counting procedure, 7 sections for each animal. An investigator blinded to the different groups performed all the analyses.

For quantification of gliosis, fluorescent images were acquired from slices stained for GFAP and Iba1 using a 20× objective (NA 0.8) with an Axio Imager 2 microscope (Zeiss) and using a 40× objective (NA 0,95) with a Spinning Disk microscope (Zeiss). After thresholding individual images (separately for GFAP and Iba1 channels), the area fraction was determined by ImageJ from 3 to 5 sections per animal and from 10 images per section as described previously (Szegő et al., 2017).

For quantification of striatal phospho-αSyn pathology, images from 3-diaminobenzidine stained sections (minimum 4 sections per animal, and minimum 4 images per section) were acquired using a 20× objective (NA 0.8) with an Axio Imager 2 microscope (Zeiss). 4 independent blinded investigators rated the pattern of phospho-αSyn signal in 40–60 randomly selected images per evaluator. Blinding was achieved by 5 digit codes. Images were rated with 0 when mostly longer segments were present, and with 1 when a punctate pattern or dotted lines dominated the image. The results were analyzed in a hierarchical nested design as previously (Szegő et al., 2012). The evaluator was set as a random factor in the generalized linear mixed model, and it had no effect on the result. From the same images, the amount of phospho-αSyn staining was quantified as area fraction of the DAB signal as described for GFAP and Iba1.

2.7. Triton X-100 solubility

For αSyn protein quantification and detection of Triton X-100 insoluble proteins, neurons were lysed in buffer containing 1% Triton X-100, 25 mM Tris pH 7.5, 150 mM NaCl, 1 mM EDTA and protease inhibitors as previously described (Szegő et al., 2019). After centrifugation (14,000 *g*, 30 min, 4 °C), supernatant was used as Triton X-100 soluble fraction. The pellet (Triton X-100 insoluble fraction) was washed in ice-cold PBS, centrifuged again and re-dissolved with sonication (10 s) in 50 μl buffer containing 2% SDS, 75 mM Tris, 15% glycerin, 3.75 mM EDTA pH 7.4 and protease inhibitors. 10 μg of Triton X-100 soluble lysate or 10 μl from the re-dissolved pellet were loaded onto a 4–20% Tris/glycine SDS gel for western blot analysis. After blocking, membranes were incubated first in the presence of antibodies against human αSyn (ALX-804-258-L001), HA tag (MMS-101P), PSD95 (3450) and alpha-tubulin (ab6046), then with horse radish peroxidase-conjugated secondary antibodies (donkey anti-rat, donkey anti-mouse and donkey anti-rabbit). Signal was visualized with chemiluminescent substrate and detected with Luminescent Image Analyzer.

2.8. Biochemical assays

To determine the toxic effect of αSyn in cultured neurons, the concentration of LDH was measured in the medium 24 h after the last

medium change using the Cytotoxicity Detection Kit (Roche) according to the manufacturer's protocol. Briefly, for each independent preparations, 3–4 technical replicates were used and averaged. Absorbances were measured at 492 nm, reference wavelength was 620 nm. Background (medium) absorbance was substracted from all values, and values were normalized to control (non-treated) and to maximal lysed (treated with 2% Triton X-100, according to the protocol) cells. Caspase activity was measured with EnzChek Caspase-3 Assay Kit (Thermo Fisher). Apoptosis was induced with 100 μM NMDA for 24 h. Cells were lysed and protein concentration determined (BCA assay). 100 μM *Z*-DEVD–AMC substrate was added to a sample of 100 μg protein. After 45 min incubation at 20 °C, fluorescence of cleaved Z-DEVD–AMC was acquired (Excitation/Emission: 342/441 nm; Infinite 200 Pro). MAP2 stained primary neurons were quantified as area fraction from 20× images as described for GFAP and Iba1.

Mitochondrial membrane potential, cytoplasmic reactive oxygen species (ROS) production and mitochondrial ROS production were measured in separate assays as described previously (Szegő et al., 2019). Tetraethylbenzimidazolylcarbocyanine iodide (JC-1, 50 nM, 37 °C, 30 min) was used to measure the mitochondrial membrane potential. Fluorescence at 485/505 nm (excitation/emission) and 535/570 nm was detected by a plate reader (Infinite 200 Pro). After measuring the basal mitochondrial membrane potential, the mitochondrial uncoupler FCCP (1 mM) was used to induce a mitochondrial stress.

Cytoplasmic ROS was measured using dichlorodihydrofluorescein diacetate (DCFH-DA; 10 mM, 37C, 30 min), mitochondrial ROS was measured using MitoSOX (200 nM, 20 min, 37C). Fluorescence at 485/530 nm (DCFH-DA) or 510/580 nm (MitoSox) was measured with plate reader. To detect the response to stress-induced ROS production, preparations were treated with 1 mM FCCP (MitoSox) or with 1% H_2O_2 (DCFH-DA).

2.9. DNA damage

To determine DNA double strand breaks, the number of 53BP1-positive nuclear loci was counted in brain sections containing nigral neurons transduced with human αSyn (minimum 3 sections per animal, and minimum 3 images per section, 15–30 neurons per animal) or in primary neuronal cultures (3 repetitions, minimum 15 neurons per repetition /condition) as previously described (Milanese et al., 2018).

DNA single- and double-strand breaks were detected via single cell gel electrophoresis (comet) assay, according to the guidelines provided in (Oliveira et al., 2006). Adherent microscopy slides were coated with 1% low melting agarose (PeqLab). Primary neurons were harvested in PBS, mixed with 1% agarose in PBS and placed on the pre-coated slide. After agarose gelling, slides were submerged in lysis buffer (2.5 M NaCl, 100 mM Na_2EDTA, 0.1% Triton X-100, 10 mM TRIS, pH 10, 4 °C, 1 h) and denatured in alkaline electrophoresis buffer (0.3 M NaOH, 1 mM Na_2EDTA, pH > 13, 30 min). Electrophoresis was carried out for 25 min at 20 V in the same buffer. Slides were removed from the electrophoresis chamber, fixed in 70% ethanol and stained with 2.5 μg/ml of propidium iodide for 20 min at 20 °C. Excess of stain was removed by rinsing the slides with distilled water. For each slide, at least 10 images were acquired using an epifluorescence microscope (Zeiss Axio Observer). For each comet, the "tail moment" was determined as the product of the percentage of DNA in the tail and the tail length using the Open Comet plugin for Image J as described previously (Paiva et al., 2017).

2.10. Statistical analysis

For in vitro experiments, "n" was set to the number of individual preparations. Within one experiment, mean of the technical replicates was determined for each treatment group. In animal experiments, "n" was set to the number of animals. No animals were excluded from the analysis. In graphs, markers represent individual preparations or individual animals, lines represent mean and standard deviation (SD) of all individual preparations or all animals. Data normality was tested by the Shapiro-Wilk test and graphically by QQ plot (R). *t*-Test, one-way ANOVA or two-way ANOVA were performed using GraphPad Prism. Linear regression was performed using R (v 2.8.0). Binomial data from pattern rating was analyzed using generalized linear mixed-effects model fitted with binomial distribution. Evaluator, animal, section and image were used as random effects nested within each other (R package: lme4). *P* values are indicated in the graphs by symbols with * or # representing $p < 0.05$, ** or ## representing $p < 0.01$, *** or ### representing $p < 0.001$. Exact *p* values are given in the Figure legend.

3. Results

3.1. Rab7 decreases αSyn toxicity in primary neuronal cultures

αSyn toxicity was induced in primary neurons by expressing human A53T αSyn via rAAV transduction on day in vitro 12 (DIV 12). Transduction with the same amount of rAAV encoding GFP was used as a control. On DIV 20, cells were fixed and stained for the neuronal marker MAP2 (Fig. 1A). The area fraction covered by MAP2-positive neurons was quantified (Fig. 1B). Cultures transduced with rAAV-αSyn presented fewer neurons and a less dense network of neurites than control cultures transduced with rAAV-GFP. In addition, cultures transduced with rAAV-αSyn released more LDH into the culture medium than cultures transduced with rAAV-GFP (Fig. 1C), indicating plasma membrane damage and cell death. Neurons transduced with rAAV-αSyn were also more vulnerable than neurons transduced with rAAV-GFP: activation of caspase-3 after exposure to excitotoxic NMDA was much more pronounced in cultures transduced with rAAV-αSyn than in cultures transduced with rAAV-GFP (Supplemental Fig. S1A—C). Caspase 3 activation was measured biochemically and using immunocytochemistry.

Next we assessed whether Rab7 is able to reduce αSyn toxicity in primary neurons by co-transducing cultures with rAAVs encoding either WT Rab7, T22N Rab7 or GFP. The Rab7 mutant T22N binds Rab7 effectors but not guanosine-5′-triphosphate (GTP). GFP was used as a negative control for the two Rab7 variants to ensure an equal amount of vector transduction and protein synthesis. Transduction with rAAV-WT Rab7 alleviated the αSyn-induced reduction in MAP2-positive area by 20% (Fig. 1A, B). With T22N Rab7, the MAP2-positive area was not significantly different from the control condition and significantly lower than with WT Rab7 (Fig. 1A, B). Similarly, the release of LDH into the culture medium was significantly decreased by transduction with rAAV-WT Rab7 (Fig. 1C). With T22N Rab7, the LDH release was not significantly different from the control condition and significantly higher than with WT RAb7 (Fig. 1C). Furthermore, the NMDA-induced caspase-3 activation was lowered by WT Rab7 (Supplemental Fig. S1A). With T22N Rab7, the NMDA-induced caspase-3 activation was not significantly different from the control condition and significantly higher than with WT Rab7 (Supplemental Fig. S1A—C).

3.2. Rab7 decreases αSyn pathology in primary neuronal cultures

To characterize αSyn pathology in our neuronal culture model, we assayed the Triton X-100 solubility of human αSyn in neuronal cell lysates (Fig. 1D-G). In lysates prepared from cultures transduced with rAAV-αSyn, human αSyn was detected both in the Triton X-100 soluble fraction (Fig. 1D) and in the Triton X-100 insoluble fraction (Fig. 1E). In lysates prepared from cultures transduced with rAAV-GFP, human αSyn was not detected in relevant amounts (Fig. 1D, E). Co-expression of WT Rab7 (detected by the HA-tag in Fig. 1D) significantly reduced the amount of Triton X-100 insoluble αSyn (Fig. 1E,F). The amount of Triton X-100 soluble human αSyn was not decreased by WT Rab7 (Fig. 1D) but rather showed a slight, but not significant increase (quantified in Supplemental Fig. S2A). With T22N Rab7, Triton X-100 insoluble αSyn was not significantly different from the control condition and significantly

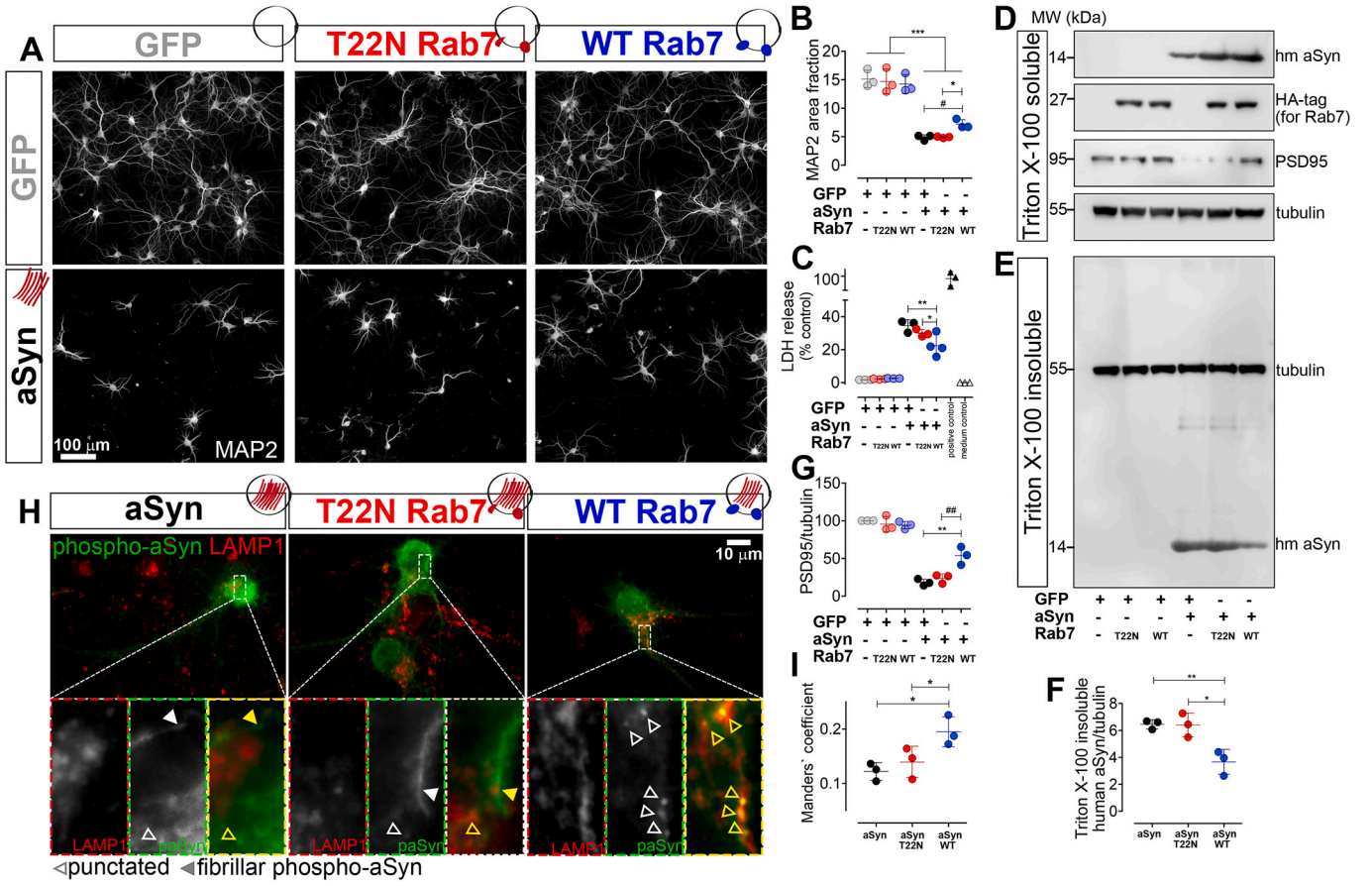

Fig. 1. WT Rab7 reduces αSyn toxicity in primary neurons.
(A) Representative images of primary neuronal cultures stained for the neuronal marker MAP2. Cultures were transduced by rAAV vectors as indicated. Scale bar: 100 µm. (B) Area fraction positive for MAP2 in cultures treated as described in (A) (markers represent $n = 3$ preparations, mean ± SD; two-way ANOVA followed by Bonferroni post-hoc test: ***: $p = 0{,}00074$; *: p = 0,0355; #: p = 0,0402). (C) LDH release was measured in cultures treated as in (A) and normalized to the indicated positive and negative controls (markers represent n = 3–4 preparations, mean ± SD; two-way ANOVA followed by Bonferroni post-hoc test, **: $p = 0{,}00064$; *: p = 0,0317). Cells of the positive control were treated with 1% Triton X-100. Empty medium was used as negative control. (D) Representative immunoblot of the Triton X-100 soluble fraction of lysates obtained from neuronal cultures as in (A). Membranes were incubated with antibodies against human αSyn, HA-tag (for Rab7), the post-synaptic marker PSD95 and the neuronal loading control βIII-tubulin. Quantification of human αSyn signal and uncroped membranes are in Supplemental Fig. S2). (E) Representative immunoblot of the Triton X-100 insoluble fraction of the neuronal lysates as in (D), run under denaturating conditions and incubated with antibodies against human αSyn and βIII-tubulin. (F) Quantification of the human αSyn signal in the Triton X-100 insoluble fraction (markers represent n = 3 blots as in (E), mean ± SD, one-way ANOVA followed by Tukey's multiple comparison test, **: $p = 0{,}0063$; *: p = 0,0271). (G) Quantification of the PSD95 signal (normalized to βIII-tubulin) from the Triton X-100 soluble fraction (markers represent n = 3 preparations as in (D), mean ± SD, two-way ANOVA followed by Bonferroni post-hoc test, **: p = 0,0061; ##: p = 0,0089). PSD95 immunostaining is in Supplemental Fig. S3. (H) Representative images of neuronal cultures transduced with rAAV as depicted and stained for phospho-αSyn (green channel) and LAMP1 (red channel). Inserts show fibrillar (closed arrowheads) and punctated (open arrowheads) phospho-αSyn signals. Scale bar: 10 µm. (I) Co-localization of phospho-αSyn and LAMP1 signals in the treated neuronal cultures expressed by the Manders` overlap coefficient (percentage of the total phospho-αSyn signal within the LAMP1 signal, n = 3 preparations, mean ± SD, one-way ANOVA, *: p = 0,0184 for αSyn vs. αSyn+WT Rab7; p = 0,0365 for αSyn+T22N Rab7 vs. αSyn+WT Rab7).

higher than with WT Rab7 (Fig. 1E, F); Triton X-100 soluble αSyn was similar to WT Rab7 (Fig. 1D, Supplemental Fig. S2A).

In order to corroborate the functional significance of αSyn aggregation on the neuronal network in culture, we quantified the amount of the postsynaptic protein PSD95 using immunoblotting (Fig. 1D,G), and the amount of PSD95 signal per neuron using immunocytochemistry (Supplemental Fig. S3). By both methods, transduction with rAAV-αSyn reduced the amount of PSD95 protein in neuronal cultures, and this effect was mitigated by WT Rab7 (Fig. 1D,G and Supplemental Fig. S3). In primary cultures transduced with rAAV-T22N Rab7, PSD95 was not significantly different from the control condition and significantly lower than with WT Rab7 (Fig. 1D, G and Supplemental Fig. S3).

Rab7 is known for orchestrating trafficking of autophagosomal and endosomal vesicles. Accordingly, we previously demonstrated in HEK293T cells that Rab7 promotes the processing of αSyn into acidic vesicles such as autolysosomes (Dinter et al., 2016). To revisit this mode of Rab7 action, we determined in our primary neuronal cultures the fraction of phospho-αSyn present in LAMP1-positive vesicles. Neurons positive for phospho-αSyn were also positive for human αSyn (Supplemental Fig. S4), indicating that the pathology resulted from transduction with rAAV-αSyn. Most neurons positive for human αSyn showed fibrillary structures positive for phospho-αSyn (closed arrowheads in Fig. 1H). These structures are reminiscent of αSyn immunoreactivity observed after PFF-induced seeding of αSyn pathology in primary neurons (Szegő et al., 2021; Volpicelli-Daley et al., 2014). In addition, we observed phospho-αSyn-positive puncta that colocalized with LAMP1 (open arrowheads in Fig. 1H). Upon quantification, the fraction of phospho-αSyn signal that colocalized with LAMP1 signal was larger in cultures transduced with rAAV-WT Rab7 than in cultures transduced with rAA T22N Rab7 (Fig. 1I). This finding is consistent with the

hypothesis that Rab7 increases maturation of αSyn-containing autophagosomes and degradation of misfolded αSyn. In line with this hypothesis, rAAV-WT Rab7 transduced neurons contained less phosphorylated αSyn compared to rAAV-T22N Rab7 or rAAV-GFP transduced neurons (Supplemental Fig. S4C).

Taken together, these findings confirmed the protective effect of WT Rab7 against αSyn pathology and the associated toxicity in mammalian neurons. The protective effects were not observed with T22N Rab7, indicating that GTP binding is necessary for this Rab7 effect. Without αSyn expression, WT Rab7 had no obvious effects on any of the measured parameters, confirming that its protective effect resulted from modulation of αSyn toxicity and not from direct, αSyn-independent

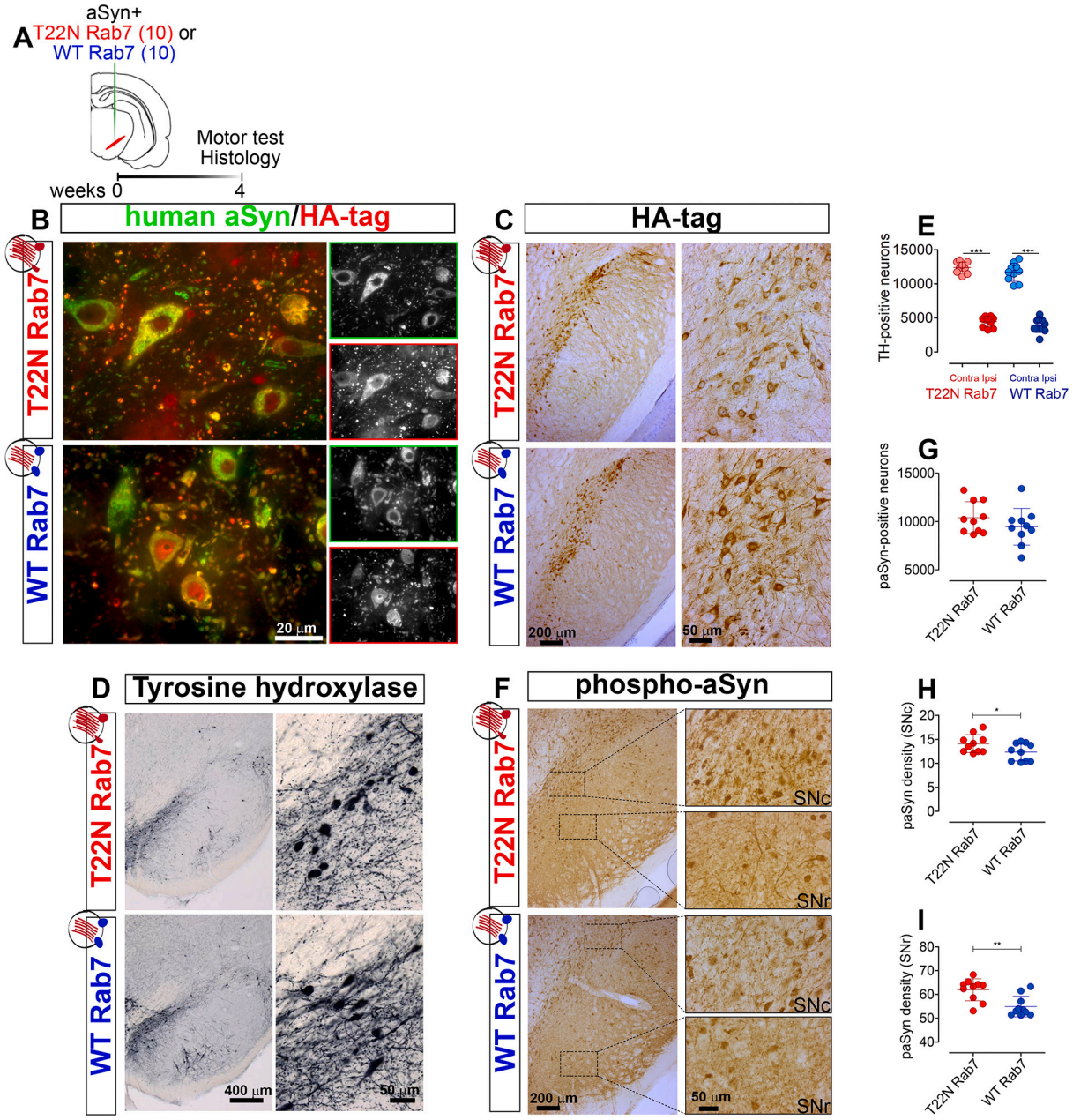

Fig. 2. WT Rab7 does not protect from loss of dopaminergic neuron somata, but reduces accumulation of phospho-αSyn in the neurophil.
(A) Experimental paradigm: rAAV encoding A53T αSyn and rAAV encoding either T22N Rab7 or WT Rab7 were injected into the right SN of rats (10 animals/group). Motor performance and αSyn-induced pathology were analyzed 4 weeks post injection. (B) Representative images of SN sections from animals injected with rAAV-αSyn and rAAV-T22N Rab7 or rAAV-αSyn and rAAV-WT Rab7 stained for human αSyn (green) and Rab7 (red, labeled through HA-tag), showing co-localization in neurons (yellow). Insets show the individual channels. Scale bar: 20 µm. (C) Representative images of SN slices stained for Rab7 (through HA-tag) in the injected hemisphere. Scale bars: 200 µm (left) and 50 µm (right). Contralateral hemispheres are in Supplemental Fig. S5A. (D) Representative images of the injected SN stained for TH. Scale bars: 400 µm (left) and 50 µm (right). Contralateral hemispheres are in Supplemental Fig. S5B. (E) Stereological quantification of the number of TH-positive neurons in the SNc of the non-injected ("contra") and injected ("ipsi") hemispheres ($n = 10$, mean ± SD, two-way ANOVA; ***: p = 0,00067; +++: p = 0,0085). (F) Representative images of SN slices of the injected hemisphere stained for phospho-αSyn. Insets show the indicated areas within the SNc (top) and SNr (bottom). Scale bars: 200 µm (left) and 50 µm (right). (G) Stereological quantification of the number of phospho-αSyn-positive neurons in the injected SNc (n = 10, mean ± SD, *t*-test). (H) Quantification of phospho-αSyn-positive structures in the neuropil of the SNc (n = 10, mean ± SD, *t*-test, p = 0,0498). (I) Quantification of phospho-αSyn-positive structures in the SNr (n = 10, mean ± SD, *t*-test, p = 0,0025). (For interpretation of the references to colour in this figure legend, the reader is referred to the web version of this article.)

effects. Transduction with rAAV-T22N Rab7 was comparable to the transduction with rAAV-GFP. In particular, T22N Rab7 expression did not cause neuronal toxicity on its own or increase the extent of αSyn pathology. Thus, even though the T22N mutant is considered dominant negative (Spinosa et al., 2008), we did not observe dominant negative effects in our paradigms.

3.3. *Rab7 does not protect dopaminergic neurons from αSyn toxicity, but it reduces the accumulation of phospho-αSyn in the substantia nigra*

In order to further validate our findings, we tested the effect of WT Rab7 on αSyn-induced toxicity in dopaminergic neurons of rat SN. To do this, animals were injected with rAAV-αSyn combined with either rAAV-WT Rab7 or rAAV-T22N Rab7 (Fig. 2A) and sacrificed for analysis four weeks after the injection. Based on our results from primary neuronal

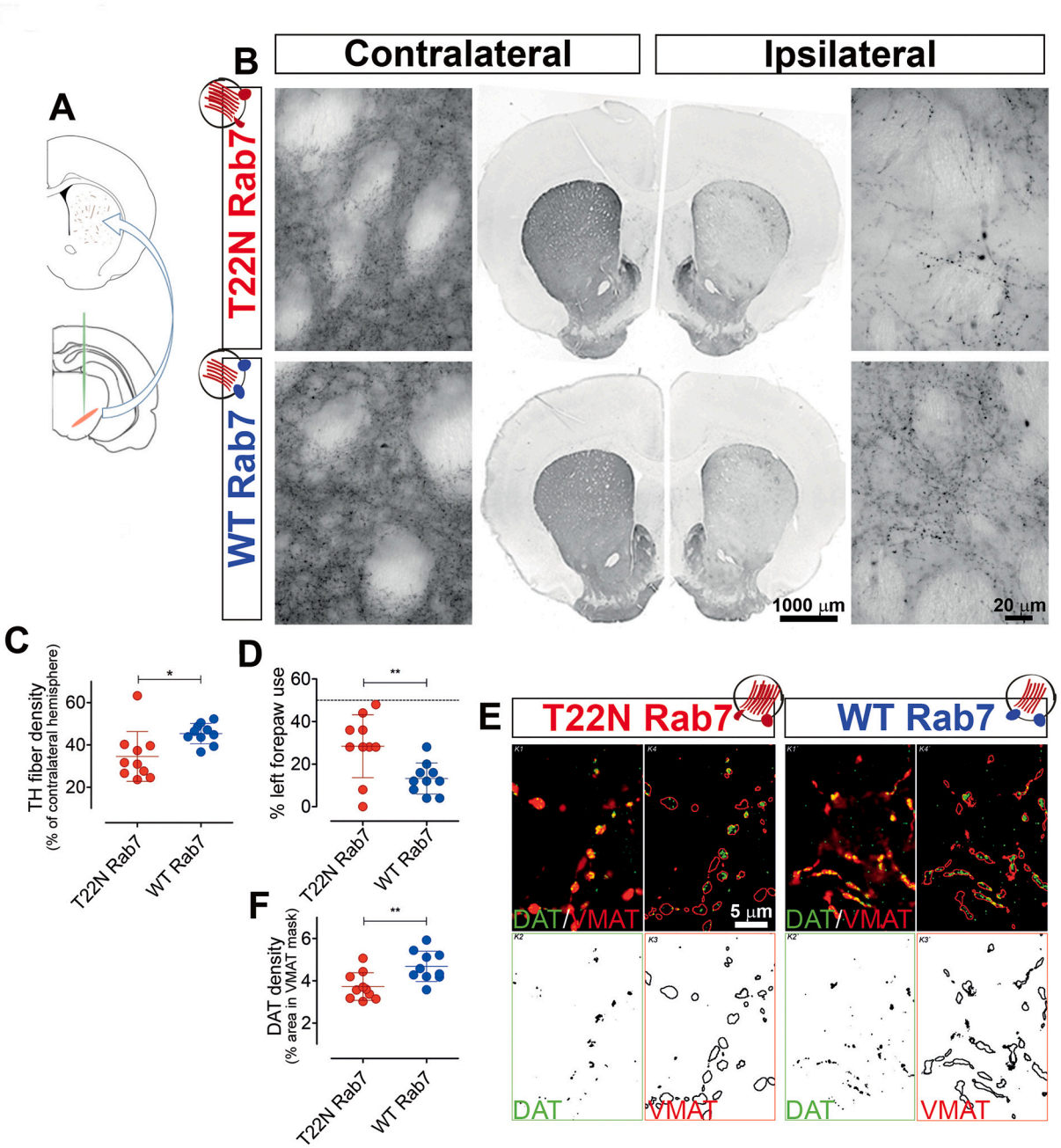

Fig. 3. WT Rab7 reduces αSyn-induced loss of dopaminergic axon terminals.
(A) Schematic presentation of the nigrostriatal pathway. Neurons in the substantia nigra were transduced by rAAV as described in Fig. 2. Dopaminergic neurons of the SNc extend their axon terminals to the striatum. (B) Representative images of striatal sections from animals injected with rAAV encoding αSyn and T22N Rab7 or αSyn and WT Rab7, stained for the dopaminergic marker tyrosine hydroxylase (TH). Scale bars: 1000 µm (center) and 20 µm (sides). (C) Quantification of the mean density of striatal dopaminergic axon terminals. Data are presented in relation to the contralateral hemisphere (n = 10, mean ± SD, *t*-test, p = 0,0149). (D) Quantification of the unilateral motor deficits 4 weeks after rAAV injection using the cylinder test (n = 10, mean ± SD, *t*-test, p = 0,0046). (E) Representative images of striatal sections stained for DAT (green pseudocolor) and VMAT2 (red pseudocolor) obtained 4 weeks after transduction with rAAV-T22N Rab7 (left) and rAAV-WT Rab7 (right) and in addition rAAV-αSyn. K1: Raw images (both channels merged). Scale bar: 5 µm. K2: Binarized DAT signal. K3: Outline mask of the binarized image from the VMAT channel. K4: Merged image of K2 and K3. (F) Quantification of the DAT signal (from images as in K2) measured in regions defined by VMAT as in K3. (area fraction, n = 10, mean ± SD, *t*-test, p = 0,0058).

cultures, we chose T22N Rab7 as the negative control for WT Rab7 in order to have transduced DNA and protein as similar as possible.

As expected, we observed in the SN of the injected hemisphere neurons positive for both human αSyn (Fig. 2B, green) and the HA-tag of Rab7 (Fig. 2B, red); most neurons were positive for both. Four weeks after the injection, the number of HA-positive neurons in the SN was not different between animals transduced with rAAV-WT Rab7 or rAAV-T22N Rab7 (Fig. 2C), and neurons with human αSyn or HA-tag expression were not observed in the contralateral hemisphere (Supplemental Fig. S5A).

Dopaminergic neurons were identified by staining for tyrosine hydroxylase (TH, Fig. 2D, Supplemental Fig. S5B). Stereological

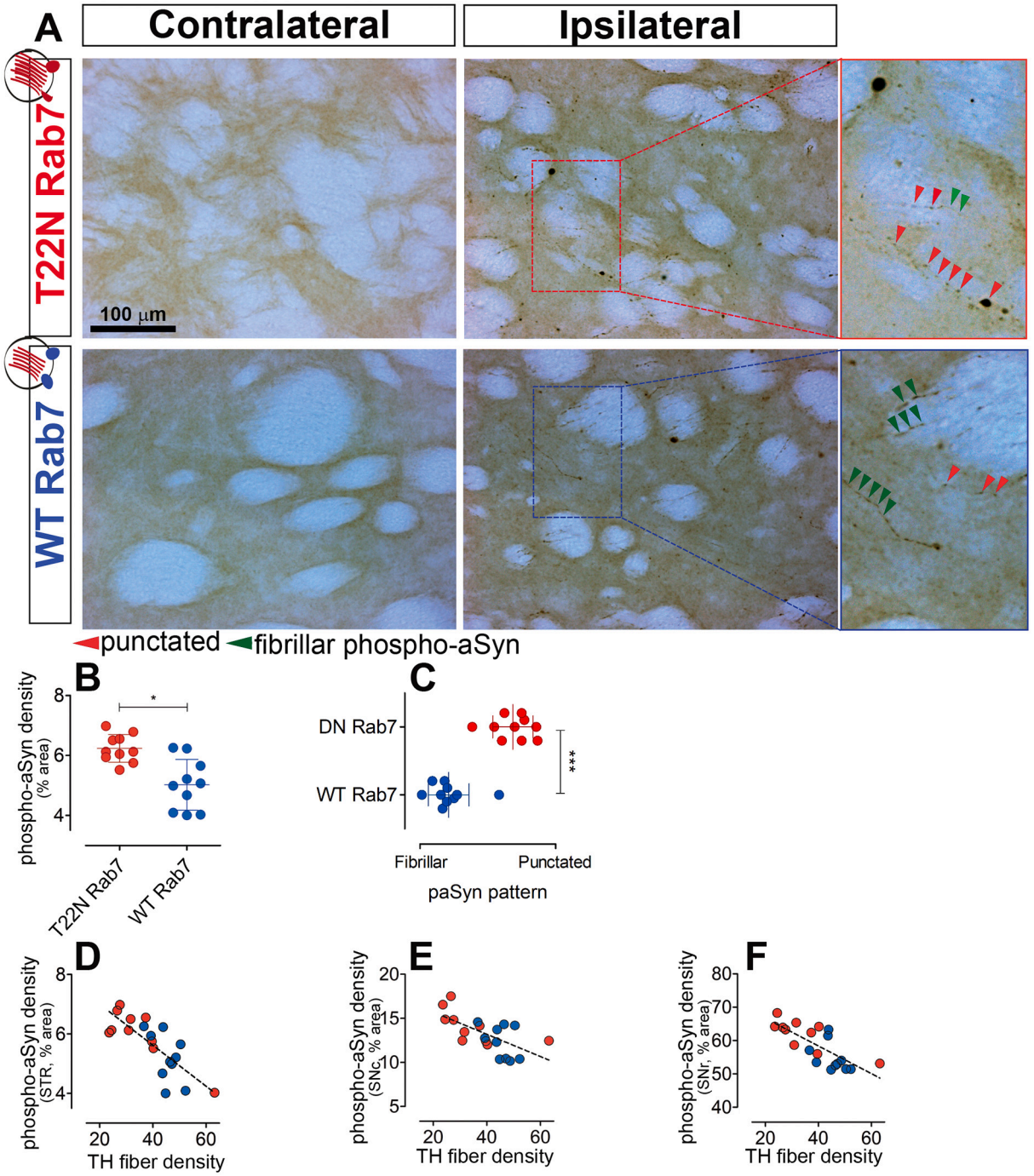

Fig. 4. WT Rab7 reduces αSyn pathology in the striatum.
(A) Representative images of striatal sections stained for phospho-αSyn. Typical fibrillar (green arrowheads) and pearl-like, punctated (red arrowheads) patterns are depicted in the inserts. Scale bar: 100 µm. (B) Quantification of the density of phospho-αSyn-positive structures in the striatum (area fraction, n = 10, mean ± SD, *t*-test, p = 0,0376). (C) Quantification of the mean rating of the phospho-αSyn-positive structures as in (A). (Binomial rating: 0 = predominantly fibrillar, 1 = predominantly pearl-like pattern; n = 10, mean ± SD, logistic regression, p = 0,00072). (D) Linear regression between the density of dopaminergic axon terminals (from Fig. 3C) and the density of phospho-αSyn structures in the striatum (from B). (p = 0,0005, r^2 = 0,6137) (E) Linear regression of dopaminergic terminals in the striatum (from Fig. 3C) with the density of phospho-αSyn structures in the substantia nigra pars compacta (from Fig. 2H). (p = 0,0022, r^2 = 0,4154) (F) Linear regression of dopaminergic terminals in the striatum (from Fig. 3C) with the density of phospho-αSyn structures in the substantia nigra pars reticulata (from Fig. 2I). (p = 0,0006, r^2 = 0,5773). (For interpretation of the references to colour in this figure legend, the reader is referred to the web version of this article.)

quantification revealed a 65% loss of TH-positive nigral neurons upon transduction with rAAV-αSyn (Fig. 2D, E). In contrast to the protective effect of WT Rab7 in cultured neurons (Fig. 1), the numbers of dopaminergic neurons were not different between animals transduced with rAAV-αSyn + rAAV-T22N Rab7 and animals transduced with rAAV-αSyn + rAAV-WT Rab7 (Fig. 2E).

Next, we analyzed the effect of Rab7 on the number of neurons in the SN that are positive for phosphorylated αSyn (Fig. 2F), a hallmark of αSyn pathology (Anderson et al., 2006). Four weeks after rAAV injection, the number of phospho-αSyn positive cells in the SN was not different between animals transduced with rAAV-αSyn + rAAV-T22N Rab7 and animals transduced with rAAV-αSyn + rAAV-WT Rab7 (Fig. 2F, G). Yet, the density of phospho-αSyn-positive structures in the area between the neurons ("neuropil") quantified in the SN pars compacta (SNc, Fig. 2H), and in the SN pars reticulata (SNr, Fig. 2I) was significantly lower in animals transduced with rAAV-WT Rab7 than in animals transduced with rAAV-T22N Rab7. We assume that a significant part of the phospho-αSyn-positive structures in the SN neuropil correspond to dendrites of dopaminergic neurons (basal dendrites in the SNc and apical dendrites in the SNr), but axonal structures and non-dopaminergic neurons could contribute to the signal as well.

3.4. Rab7 protects striatal dopaminergic axon terminals from αSyn toxicity

Next, we characterized the effect of WT Rab7 and T22N Rab7 on the αSyn-induced loss of dopaminergic axon terminals ("fibers") in the striatum (Fig. 3A, B). In both groups, the density of striatal dopaminergic fibers was reduced to less than half of the density in the contralateral, non-injected hemisphere. Yet, the reduction was less pronounced in animals transduced with rAAV-αSyn + rAAV-WT Rab7 than in animals transduced with rAAV-αSyn + rAAV-T22N Rab7 (Fig. 3B, C). This 16% rescue is consistent with the protective effect of WT Rab7 on the density of the neuronal network in cultured neurons (Fig. 1B) and with the reduced density of phospho-αSyn in the SN neuropil (Fig. 2F). The extent of fiber loss in the striatum did not correlate with the loss of somata in the SN of the same animals (Supplemental Fig. S5C), but a differing response to toxic insults by somata of dopaminergic neurons in the SN and their axonal compartments in the striatum has been observed in numerous previous studies (Chung et al., 2009; Koch et al., 2015; Masliah et al., 2000).

Striatal αSyn pathology was observed only in the injected hemisphere (Fig. 4A). It was mostly detected along neurite-like structures (Fig. 4A, insets, green arrows). Double staining for phospho-αSyn and TH revealed an overlapping distribution (Supplemental Fig. S5D), confirming that the majority of phospho-αSyn in the striatum is localized in dopaminergic terminals. We observed both fibrillar phospho-αSyn staining patterns (Fig. 4A, green arrowheads) and punctuated phospho-αSyn staining patterns (red arrowheads) and assume that the punctuated pattern represents a more advanced stage of neurite degeneration. The overall density of phospho-αSyn-positive structures was significantly lower in animals transduced with rAAV-WT Rab7 compared to animals transduced with rAAV-T22N Rab7 (Fig. 4B). In addition, we determined qualitatively whether images showed predominantly a fibrillary or punctuated phospho-αSyn staining pattern. These blinded ratings revealed that the more advanced punctuated pattern was more prevalent in animals transduced with rAAV-T22N Rab7, while animals transduced with rAAV-WT Rab7 showed more of the fibrillary pattern (Fig. 4C). These findings are in line with the observed protective effect of WT Rab7 on the striatal dopaminergic axonal terminals (Fig. 3C), the reduced amount of Triton X-100 insoluble αSyn in cultured neurons (Fig. 1E), the differences in phospho-αSyn-positive dendrites in SNc and SNr (Figs. 2H, I), and with our previous finding that WT Rab7 can promote the degradation of αSyn aggregates (Dinter et al., 2016).

The significant negative correlation between the amount of striatal phospho-αSyn and the density of dopaminergic fibers (Fig. 4D) suggests that αSyn pathology is closely linked to the degeneration of axon terminals. The strong correlation between the density of striatal dopaminergic fibers in each animal and the amount of phospho- αSyn in the SNc (Fig. 4E) and SNr (Fig. 4F) indicates that αSyn pathology affects the entire neuron.

Next, we assessed whether Rab7 affected motor performance. Forelimb use is regulated by the extracellular concentration of dopamine in the contralateral striatum. αSyn-induced motor deficits were therefore quantified by the cylinder test, carried out four weeks after rAAV injection. Unilateral transduction with rAAV-αSyn combined with either rAAV-WT Rab7 or rAAV-T22N Rab7 into the right hemisphere reduced left forepaw use in almost all animals (Fig. 3D), consistent with the fact that dopamine is secreted from nigrostriatal axon terminals and TH fibers were reduced in the right striatum (Fig. 3C). Surprisingly, the forelimb asymmetry was larger in animals transduced with rAAV-WT Rab7 than in animals transduced with rAAV-T22N Rab7 (Fig. 3D). This finding was unexpected given the blunted TH fiber loss with WT Rab7 (Fig. 3C). However, it could be explained by an effect of Rab7 on the dopamine transporter (DAT) (Eriksen et al., 2010; Wu et al., 2017). The DAT is responsible for dopamine reuptake and termination of dopamine signaling. Reduced DAT activity potentiates dopaminergic neurotransmission and can cause asymmetry in forelimb use (Lee et al., 2008). We co-stained striatal sections for DAT and vesicular monoamine transporter 2 (VMAT2) (Fig. 3E). The area of the DAT signal within VMAT2-positive fibers was significantly higher in animals transduced with rAAV-WT Rab7 than in animals transduced with rAAV-T22N Rab7 (Fig. 3F). This finding can potentially explain the observed asymmetry in forelimb use.

αSyn pathology induces the activation of glia cells, which can induce toxic as well as protective responses (Nichols et al., 2019; Pekny et al., 2014). Transduction with rAAV-αSyn induced microglia activation in the injected striatum, but there was no difference between animals transduced with WT Rab7 and T22N Rab7 (Supplemental Fig. S6A, B). For astroglia, the αSyn-induced activation was moderate in animals with T22N Rab7 and significantly higher in animals with WT Rab7 (Supplemental Fig. S6A, C). Yet, the lacking correlation between the astroglia reaction and dopaminergic fiber density (Supplemental Fig. S6D) argues against a direct role of astroglia.

3.5. Rab7 reduces αSyn-induced fiber loss by increasing viability of dopaminergic neurons

It is well established that dopaminergic axon terminals regenerate after toxic insults (Kowsky et al., 2007), and that αSyn can inhibit this regeneration (Szegő et al., 2012). In order to rule out that the differences in the density of striatal dopaminergic terminals in Fig. 3C results from differences in axon terminal regeneration, we investigated whether WT Rab7 affects axon regrowth. Primary neurons were seeded in microfluidic chambers that separate axons from somata. After rAAV transduction, axons were dissected and the length of regenerated axons was measured five days later. Neither T22N Rab7 nor WT Rab7 alone had an effect on regeneration (Supplemental Fig. S7). In contrast, αSyn significantly reduced axon regeneration. The length of regenerated axons was shorter in cultures transduced with WT Rab7 and αSyn than in cultures transduced with T22N Rab7 and αSyn. Differences in axon sprouting therefore do not account for the differences between the densities of dopaminergic terminals in rat striatum.

Accumulation of human αSyn impairs neuronal viability and neuronal functioning, which, in turn, causes further accumulation of toxic αSyn species. Therefore, mitigation of αSyn pathology by WT Rab7 overexpression should improve cellular functioning, increase viability and slow down neurite retraction. To test this hypothesis, we measured the amount of reactive oxygen species (ROS) and the mitochondrial membrane potential, two classical indicators of cellular functioning (Musgrove et al., 2019) in primary neurons transduced with rAAV-αSyn and rAAV-Rab7. ROS levels and the mitochondrial membrane potential

were normalized to control cultures transduced only by rAAV-GFP (represented as dashed lines in Figs. 5A-C). Cultures transduced with rAAV-αSyn showed about 20% more basal cytosolic ROS than cultures without αSyn (Fig. 5A), consistent with our earlier findings (Szegő et al., 2019). αSyn increased mitochondrial ROS to a similar extent (Fig. 5B), and reduced the mitochondrial membrane potential (Fig. 5C). In addition to these steady-state measurements, we tested neurons' response to an acute induction of oxidative and mitochondrial stress: Treatment with H_2O_2 increased cytoplasmic ROS beyond the extent observed with αSyn transduction alone (Fig. 5A). Similarly, treatment with the mitochondrial uncoupler FCCP increased mitochondrial ROS (Fig. 5B) and decreased the mitochondrial membrane potential (Fig. 5C).

The αSyn-induced increase in steady-state cytoplasmic ROS was not significantly affected by Rab7 (Fig. 5A), but handling stress-induced ROS was more efficient in cultures transduced with rAAV-WT Rab7 than in cultures transduced with rAAV-GFP or rAAV-T22N Rab7 (Fig. 5A). For mitochondrial ROS, both steady-state and stress-induced levels of mitochondrial ROS were lower in cultures transduced with rAAV-WT Rab7 than in cultures transduced with rAAV-GFP or rAAV-T22N Rab7 (Fig. 5B). Finally, transduction with rAAV-WT Rab7 stabilized the mitochondrial membrane potential as compared to rAAV-GFP and rAAV-T22N Rab7 - and mitigated the stress-induced reduction in the mitochondrial membrane potential (Fig. 5C). These findings suggest that the protective effects of WT Rab7 observed in cultured neurons and in the striatum could involve better handling of αSyn-induced oxidative damage and less mitochondrial impairment. In none of the measurements did T22N Rab7 differ from GFP (Fig. 5A-C), confirming that T22N Rab7 does not induce additional toxicity in this paradigm.

Aggregated αSyn and ROS induce DNA damage (Martin et al., 2006; Milanese et al., 2018; Paiva et al., 2017; Schaser et al., 2019). We therefore measured αSyn-induced DNA damage by the comet assay. Nuclei of neurons transduced with rAAV-GFP instead of rAAV-αSyn remained intact during electrophoresis (Fig. 5D), whereas a significant amount of fragmented DNA was mobilized into comet tails from nuclei of rAAV-αSyn transduced neurons (Fig. 5D). The αSyn-induced tail moment was significantly decreased by co-transduction with rAAV-WT Rab7 as compared to transduction with rAAV-GFP or rAAV-T22N Rab7 (Fig. 5D, E).

DNA breaks recruit specific repair proteins to the sites of the damage. Tumor suppressor p53-binding protein 1 (53BP1) is an effector of the canonical DNA damage response (Panier and Boulton, 2014), and 53BP1 foci can be used to quantify the extent of DNA damage. The number of 53BP1 foci was significantly higher in neurons transduced with rAAV-αSyn than in neurons transduced with the rAAV-GFP control (Fig. 5F, G). WT Rab7, but not T22N Rab7, reduced the number of 53BP1 foci (Fig. 5G), confirming the reduction of DNA fragmentation as reported by the comet assay (Fig. 5E). Both methods also confirmed that expression of T22N Rab7 per se did not induce DNA damage in neurons.

To confirm these Rab7 effects obtained in neuronal cultures, we determined the effect of αSyn and Rab7 on DNA damage in rat brain by quantifying the number of 53BP1 foci in neurons of rat SN (Fig. 6). Transduction with rAAV-αSyn increased the number of 53BP1 foci in SN neurons, and fewer 53BP1 foci were observed in animals transduced with rAAV-WT Rab7 than with rAAV-T22N Rab7 (Fig. 6A, B). The extent of DNA damage as reported by the number of 53BP foci correlated with the density of dopaminergic axon terminals in the striatum of the same animal (Fig. 6C), and similarly with the amount of phospho-αSyn in striatum (Fig. 6D), SNr (Fig. 6E) and SNc (Fig. 6F). These correlations confirm the close link between degeneration of axon terminals, aggregate load and DNA damage. In conclusion they suggest that WT Rab7 reduces DNA damage by reducing αSyn aggregates.

4. Discussion

Here we report that the expression of WT Rab7 reduced αSyn pathology in primary neurons and in the rodent brain. Transduction with rAAV-WT Rab7 abated αSyn-induced pathology. Primary cultures showed a higher density of MAP2-positive neurons and PSD95-positive synapses. They also showed decreased LDH release and caspase-3 activation. In animals, the lesion of dopaminergic axon terminals in the rat striatum and the extent of αSyn pathology were smaller. Pathological αSyn was decreased, and the fraction of αSyn in lysosomal vesicles increased by Rab7, indicating that toxic αSyn species are reduced via autolysosomal clearance. WT Rab7 reduced αSyn-induced ROS production, mitochondrial impairment and DNA damage, confirming the functional relevance of reducing αSyn pathology.

We induced αSyn pathology and toxicity by overexpressing A53T αSyn in the SN of rats and in primary mouse neurons using rAAV. Overexpression of αSyn in the rat brain induced a robust phenotype with a 60% reduction of both the number of dopaminergic somata in the SN (Fig. 2E) and dopaminergic axon terminals in the striatum (Fig. 3C) – in line with previous reports (Van der Perren et al., 2015). To promote the autolysosomal degradation of toxic αSyn species and to reduce αSyn dependent phenotypes, we expressed WT Rab7. The T22N mutant of Rab7 was used as a negative control. With WT Rab7, the densities of phospho-αSyn positive structures in SNc and SNr were reduced (Fig. 2), as was the density of phospho-αSyn positive axon terminals in the striatum (Fig. 4). In primary neurons, we observed a reduced amount of αSyn in the Triton X-100 insoluble fraction (Fig. 1E, F) and a higher colocalization between phospho-αSyn and LAMP1 with WT Rab7 compared to T22N Rab7 or GFP (Fig. 1H, I), indicating that Rab7 promotes the fusion of αSyn containing autophagosomes with lysosomes. This is consistent with our previous finding that Rab7 increases the fraction of αSyn in autolysosomes as reported by RFP-GFP tandem fluorescence (Dinter et al., 2016), and with the known promotion of autophagosome maturation by Rab7 (Gutierrez et al., 2004; Jäger et al., 2004; Wang et al., 2016a; Zhan et al., 2017; Zhao and Zhang, 2019).

T22N Rab7 did not increase the accumulation of insoluble αSyn (Fig. 1E, F) or induce toxicity (Fig. 1B, C, Fig. 5). This finding was unexpected given the reported dominant negative effects of the T22N mutation. It can be explained by assuming that Rab7 dependent aggregate clearance operates at low capacity without rAAV transduction (hence it cannot be reduced further by T22N Rab7). This hypothesis explains the lacking negative effect of T22N Rab7 and also the moderate but significant stimulation of aggregate clearance by transduction with rAAV-WT Rab7. A low baseline extent of Rab7-dependent aggregate clearance is consistent with the fact that there is no direct evidence that PD can be caused by a deficit in Rab7 activity except for the observation that mutations in the RAB7 gene are associated with melanoma (Alonso-Curbelo et al., 2014), which is more common in PD patients. Still, several other proteins involved in trafficking of endosomes and autophagosomes are linked to PD, including RabGEF1 and Arl8b (Bandres-Ciga et al., 2019). RabGEF1 activates Rab5 (Horiuchi et al., 1997) which characterizes early endosomes and is subsequently exchanged for Rab7. Both Rab7 and Arl8 are localized on late endosomes (Horiuchi et al., 1997; Jongsma et al., 2020; Marwaha et al., 2017), and Rab7 is exchanged for Arl8 during endosome maturation (Jongsma et al., 2020). Thus, the autophago-lysosomal pathway is clearly important during PD pathogenesis, and stimulating autophagosome maturation can be a viable therapeutic strategy even without a causative role of Rab7 during PD pathogenesis.

What is the mechanism of Rab7-induced aggregate clearance? Factors that mediate the Rab7 effects include the centrosomal protein ninein-like protein (Nlp), which enhances the interaction between Rab7 and FYCO1 (Xiao et al., 2021), PLEKHM1 (Marwaha et al., 2017) and Arl8 (Marwaha et al., 2017). Furthermore, we previously demonstrated that FYCO1 mediates the effect of Rab7 on the clearance of αSyn aggregates in HEK293T cells and in the fruit fly (Saridaki et al., 2018). Yet, the cellular mechanis underlying this effect has remained unclear. Rab7 primarily regulates autophagosome transport and fusion with lysosomes (Gutierrez et al., 2004; Jäger et al., 2004; Wang et al., 2016a; Zhao and Zhang, 2019). More recently, Rab7 has been implicated in the formation

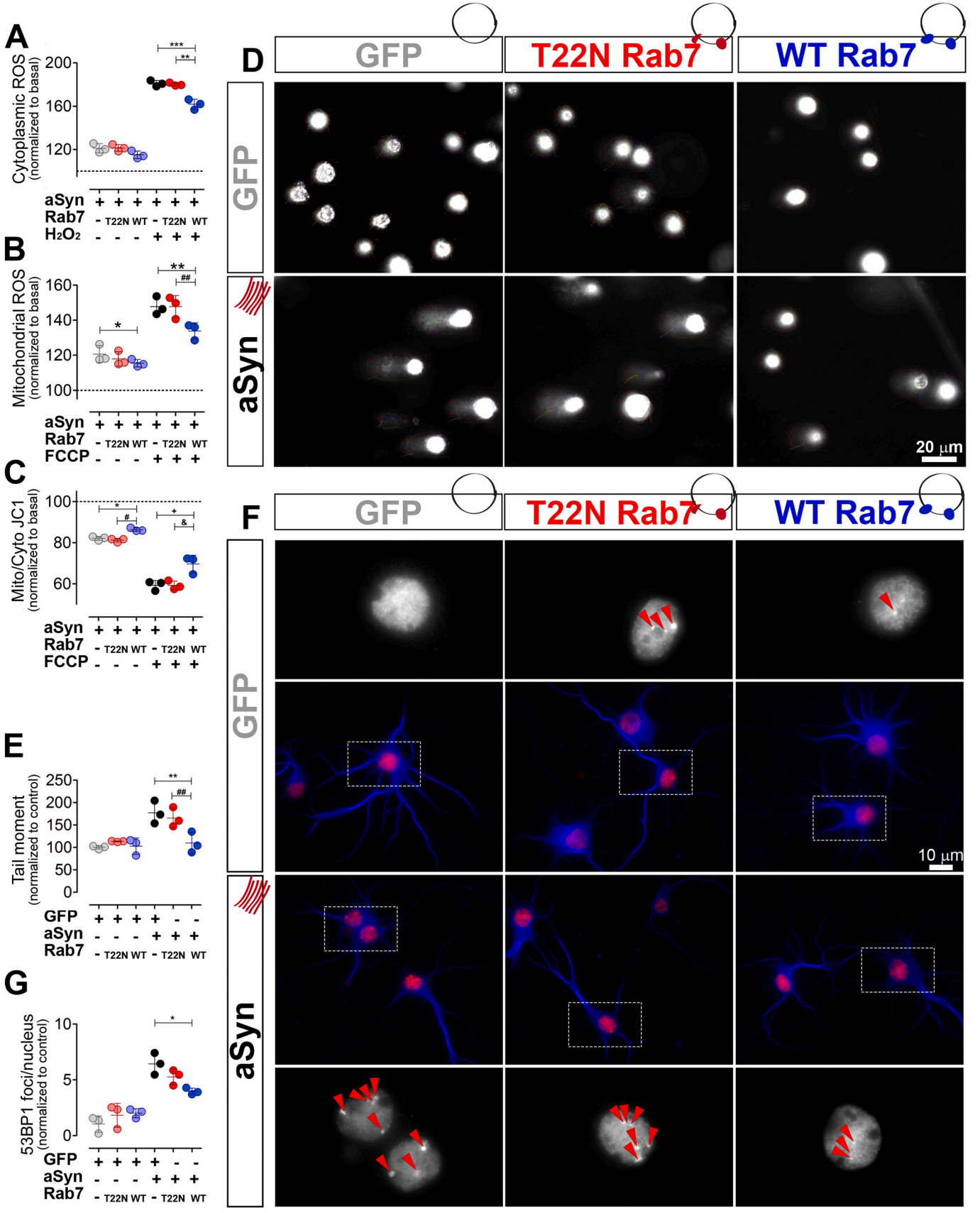

(caption on next page)

Fig. 5. WT Rab7 mitigates αSyn-induced oxidative stress and DNA damage in primary neurons.
(A-G) Primary neuronal cultures were transduced with rAAV encoding αSyn or GFP and in addition with rAAV encoding GFP, T22N Rab7 or WT Rab7 and analyzed four days (DNA repair site visualized by 53BP1, biochemical assays) or eight days (comet assay) later. (A) Cytoplasmic ROS determined using DCFH-DA and expressed relative to the mean of all control cultures (i.e. all cultures transduced with GFP instead of αSyn), represented by the dotted line. The "-"in the row for Rab7 stands for GFP. Additional oxidative stress was induced by adding 1% H_2O_2 where indicated (n = 3, mean ± SD, ANOVA followed by Bonferroni posthoc test; ***: p = 0,00068; **: p = 0,0071). (B) Mitochondrial ROS determined using MitoSOX and expressed relative to the mean of all control cultures (dotted line). Additional mitochondrial ROS were induced by adding 1 mM FCCP where indicated. (n = 3, mean ± SD, ANOVA followed by Bonferroni posthoc test; *: p = 0,0408; ##: p = 0,0058; **: p = 0,0069). (C) Mitochondrial membrane potential measured by JC-1 expressed relative to the mean value of all control conditions (dotted line). FCCP was added where indicated (n = 3, mean ± SD, ANOVA followed by Bonferroni posthoc test; *: p = 0,0433; #: p = 0,0395; +: p = 0,0296; &: p = 0,0247). (D) Representative images of comet assays, i.e. neuronal nuclei embedded in agarose and stained by propidium iodide after electrophoresis. Scale bar: 20 μm. (E) Mean tail moments determined for each preparation from minimal 10 images per preparation as in (D) (n = 3, mean ± SD, ANOVA followed by Bonferroni posthoc test; **: p = 0,00317; ##: p = 0,0053). (F) Representative images of primary neurons stained for the DNA damage response protein 53BP1 (red) and MAP2 (blue) showing 53BP1-positive foci in the nuclei (red arrowheads) representing DNA damage sites. Scale bar: 10 μm. Boxes depict the areas shown in the insets above and below the image. In the insets, only the 53BP1 channel is shown. (G) Mean number of 53BP1-foci per nucleus for each preparation obtained from minimal 15 neurons per condition (n = 3, mean ± SD, ANOVA followed by Bonferroni posthoc test; p = 0,0109). (For interpretation of the references to colour in this figure legend, the reader is referred to the web version of this article.)

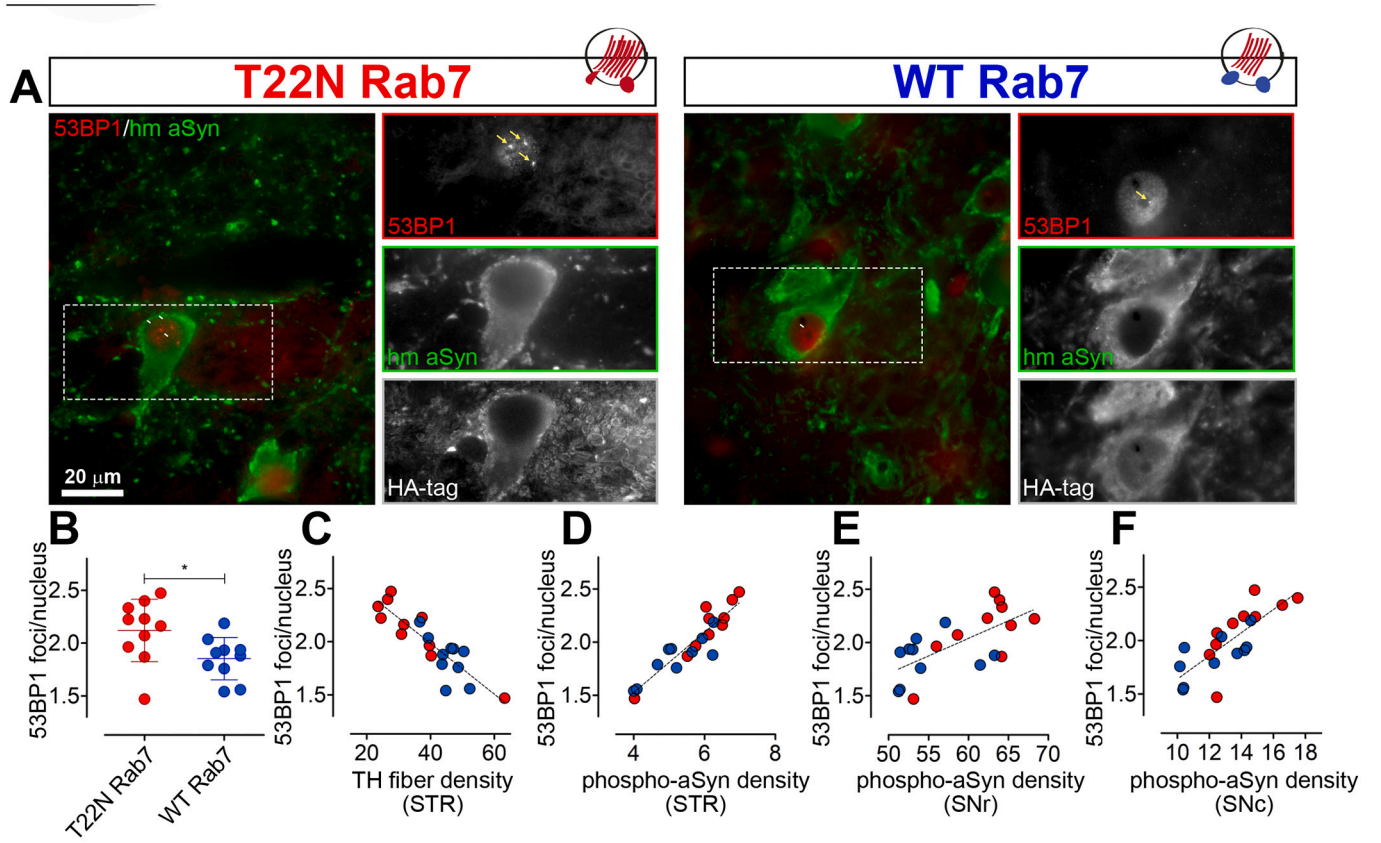

Fig. 6. WT Rab7 mitigates αSyn-induced DNA damage in the substantia nigra.
(A) Representative images of substantia nigra slices stained for 53BP1 (red, top insert), human αSyn (green, middle insert) and Rab7 (HA tag, bottom insert), obtained from animals treated as described in Fig. 2A. Boxes are enlarged in the insets. DNA damage sites a depicted by yellow arrows. Scale bar 20 μm. (B) Average number of 53BP1-foci per nucleus determined from images as in (A) and 15–30 neurons per animal (n = 10, mean ± SD, *t*-test, p = 0,0148). (C—F) Linear regression of the number of DNA damage sites (from B) with the density of dopaminergic axon terminals in the striatum (C, from Fig. 3C, p = 0,0001, r^2 = 0,7725), the density of phospho-αSyn structures in the striatum (D, from Fig. 4B, p = 0,00011, r^2 = 0,8432), the density of phospho-αSyn structures in the substantia nigra pars reticulata (E, from Fig. 2I, p = 0,00015, r^2 = 0,4304) and the density of phospho-αSyn structures in the pars compacta (F, from Fig. 2H, p = 0,00014, r^2 = 0,6108). Markers represent individual animals, *n* = 10. (For interpretation of the references to colour in this figure legend, the reader is referred to the web version of this article.)

of membrane contact sites between the ER and autophagosomes (Elbaz-Alon et al., 2020) and in cholesterol transport (Meneses-Salas et al., 2020; van den Boomen et al., 2020). These processes could therefore contribute to Rab7-induced aggregate clearance.

Because Rab7 is a major signaling hub (Langemeyer et al., 2018; Wen et al., 2017; Zhang et al., 2009), directly increasing its activity might induce several off-target effects. One such off-target effect of Rab7 could explain our behavioral finding (Fig. 3J): Since Rab7 regulates endosomal trafficking, it could affect the abundance of DAT in striatal axon terminals - as suggested by the findings in Fig. 3F. Specifically, higher DAT abundance in striatal axon terminals of animals transduced with WT Rab7 (Fig. 3F) could result in accelerated dopamine clearance and explain the reduced forelimb use (Fig. 3D). However, further experimental data is necessary to confirm this. In addition, the DAT is a secondary active transporter. Improved neuronal health in neurons transduced with WT Rab7 - as suggested by less DNA damage and better mitochondrial function - can also explain increased dopamine clearance and reduced forelimb use. Along similar lines, altered striatal dopamine

clearance underlies the paradoxically improved motor performance in a mouse model of αSyn pathology (Hunn et al., 2019). These observations highlight the Janus-faced consequences of dopaminergic terminal loss in the striatum: On the one hand, fewer terminals secrete less dopamine. On the other hand, reduced dopamine clearance and receptor sensitisation potentiate dopamine effects. Accordingly, dyskinesias are induced more easily in dopamine-denervated striatum, and experimentally increasing striatal DAT activity can reduce dyskinesias (Tomas et al., 2016).

We observed a tight correlation between (1) the degeneration of dopaminergic terminals in the striatum, (2) αSyn pathology and (3) DNA damage (Fig. 4D, E and Fig. 6C, D). The fact that corresponding values for animals treated with either WT Rab7 or T22N Rab7 aligned on the same regression curve suggests that the protection of dopaminergic axon terminals by WT Rab7 was achieved by the reduction of αSyn pathology and the subsequent reduction of DNA damage. Cellular functioning and αSyn pathology are intricately linked, and the individual pathogenic steps potentiate each other. Our findings suggest that stimulating the rate limiting step of autolysosomal αSyn aggregate clearance by rAAV-mediated WT Rab7 expression breaks this vicious circle, and the improved cellular functioning limits further αSyn aggregation.

5. Conclusion

WT Rab7 reduced αSyn-induced degeneration of primary neurons and striatal dopaminergic axon terminals. WT Rab7 also lowered αSyn pathology and associated toxicity, including oxidative stress, mitochondrial impairment and DNA damage. These findings confirm that improving autophagosome maturation is a possible therapeutic strategy for PD.

Supplementary data to this article can be found online at https://doi.org/10.1016/j.expneurol.2021.113900.

Ethical approval and consent to participate

Animals were approved by local authorities (Bioethical Committee of the KU Leuven, Belgium, ECD project P067-2013 and P085-2014; Landesdirektion Sachsen, Germany, project 25-5131/476/15) and conducted in accordance with guidelines of the Federation for European Laboratory Animal Science Associations (FELASA).

Consent for publication

All authors approved the manuscript.

Availability of data and materials

The dataset supporting the conclusions of this article is included within the article and its additional files.

Funding

This work was supported by the German Research Foundation (DFG to BF, FA 658/3-1) and by the FWO (postdoctoral fellowship to AVDP and project G080517N), the KU Leuven (C14/18/102), the Medical Foundation Queen Elisabeth and the ERA-NET JPco-fuND 2015 SYNACTION.

Authors' contributions

AVDP, VB and BF conceived research. EMSz, CVDH, LH, AVDP performed research. EMSz, AVDP and BF wrote the manuscript, all authors contributed and approved the manuscript.

Declaration of Competing Interest

The authors declare that they have no competing interests.

Acknowledgements

We thank Sabine Hamm, Anett Böhm, Andrea Kempe and Annelies Aertgeerts for excellent technical assistance.

References

Alonso-Curbelo, D., Riveiro-Falkenbach, E., Pérez-Guijarro, E., Cifdaloz, M., Karras, P., Osterloh, L., Megías, D., Cañón, E., Calvo, T.G., Olmeda, D., Gómez-López, G., Graña, O., Sánchez-ArévaloLobo, V.J., Pisano, D.G., Wang, H.W., Ortiz-Romero, P., Tormo, D., Hoek, K., Rodríguez-Peralto, J., Joyce, J.A., Soengas, M.S., 2014. RAB7 controls melanoma progression by exploiting a lineage-specific wiring of the endolysosomal pathway. Cancer Cell 26, 61–76.

Anderson, J.P., Walker, D.E., Goldstein, J.M., De Laat, R., Banducci, K., Caccavello, R.J., Barbour, R., Huang, J., Kling, K., Lee, M., Diep, L., Keim, P.S., Shen, X., Chataway, T., Schlossmacher, M.G., Seubert, P., Schenk, D., Sinha, S., Gai, W.P., Chilcote, T.J., 2006. Phosphorylation of Ser-129 is the dominant pathological modification of α-synuclein in familial and sporadic lewy body disease. J. Biol. Chem. 281, 29739–29752.

Baba, T., Toth, D.J., Sengupta, N., Kim, Y.J., Balla, T., 2019. Phosphatidylinositol 4,5-bisphosphate controls Rab7 and PLEKHM 1 membrane cycling during autophagosome–lysosome fusion. EMBO J. 38.

Baekelandt, V., Claeys, A., Eggermont, K., Lauwers, E., De Strooper, B., Nuttin, B., Debyser, Z., 2002. Characterization of lentiviral vector-mediated gene transfer in adult mouse brain. Hum. Gene Ther. 13, 841–853.

Bandres-Ciga, S., Saez-Atienzar, S., Bonet-Ponce, L., Billingsley, K., Vitale, D., Blauwendraat, C., Gibbs, J.R., Pihlstrøm, L., Gan-Or, Z., Noyce, A.J., Kaiyrzhanov, R., Middlehurst, B., Kia, D.A., Tan, M., Houlden, H., Morris, H.R., Plun-Favreau, H., Holmans, P., Hardy, J., Trabzuni, D., Bras, J., Quinn, J., Mok, K.Y., Kinghorn, K.J., Wood, N.W., Lewis, P., Schreglmann, S., Guerreiro, R., Lovering, R., RụBibo, L., Rizig, M., Ryten, M., Guelfi, S., Escott-Price, V., Chelban, V., Williams, N., Morrison, K.E., Brice, A., Danjou, F., Lesage, S., Corvol, J.C., Martinez, M., Schulte, C., Brockmann, K., SimƀBn-Sẓnchez, J., Heutink, P., Rizzu, P., Sharma, M., Gasser, T., Nicolas, A., Cookson, M.R., Craig, D.W., Faghri, F., Hernandez, D.G., Shulman, J.M., Iwaki, H., Leonard, H.L., Nalls, M.A., Robak, L., Lubbe, S., Finkbeiner, S., Mencacci, N.E., Singleton, A.B., Reed, X., Alcalay, R.N., Rouleau, G.A., van Hilten, J.J., Adarmes-GƀmezA.D., Aguilar, M., Alvarez, I., Alvarez, V., Barrero, F.J., Yarza, J.A.B., Bernal-Bernal, I., Blazquez, M., Bonilla-Toribio, M., Botɲa, J.A., Boungiorno, M.T., Buiza-Rueda, D., Cẓmara, A., Carrillo, F., CarriƀBn-Claro, M., Cerdan, D., ClarimƀBn, J., Compta, Y., de la Casa, B., Diez-Fairen, M., Dols-Icardo, O., Duarte, J., Duran, R., Escamilla-Sevilla, F., Ezquerra, M., Feliz, C., Fernẓndez, M., Fernẓndez-Santiago, R., Garcia, C., Garcɲa-Ruiz, P., GƀmezGarre, P., Heredia, M.J.G., Pagola, A.G., Infante, J., Jimenez-Escrig, A., Kulisevsky, J., Labrador-Espinosa, M.A., Lopez-Sendon, J.L., de Munain Arregui, A. L., Torres, I.M., Marɲn, J., Marti, M.J., Martɲnez-Castrillo, J.C., Mȳndez-del-Barrio, C., Gonzẓlez, M.M., Mata, M., Mɲnguez, A., Mir, P., Rezola, E.M., Muʔoz, E., Pagonabarraga, J., Pascual-Sedano, B., Pastor, P., Errazquin, F.P., Periẓn-Tocino, T., Ruiz-Martɲnez, J., Ruz, C., Rodriguez, A.S., Sierra, M., Suarez-Sanmartin, E., Tabernero, C., Tartari, J.P., Tejera-Parrado, C., Tolosa, E., Valldeoriola, F., Vargas-Gonzẓlez, L., Vela, L., Zimprich, A., Pihlstrom, L., Toft, M., Koks, S., Taba, P., Hassin-Baer, S., 2019. The endocytic membrane trafficking pathway plays a major role in the risk of Parkinson's disease. Mov. Disord. 34, 460–468.

Burgoyne, J.R., 2018. Oxidative stress impairs autophagy through oxidation of ATG3 and ATG7. Autophagy 14 (6), 1092–1093.

Chang, D., Nalls, M.A., Hallgrímsdóttir, I.B., Hunkapiller, J., van der Brug, M., Cai, F., Kerchner, G.A., Ayalon, G., Bingol, B., Sheng, M., Hinds, D., Behrens, T.W., Singleton, A.B., Bhangale, T.R., Graham, R.R., 2017. A meta-analysis of genome-wide association studies identifies 17 new Parkinson's disease risk loci. Nat. Genet. 49, 1511–1516.

Chung, C.Y., Koprich, J.B., Siddiqi, H., Isacson, O., 2009. Dynamic changes in presynaptic and axonal transport proteins combined with striatal neuroinflammation precede dopaminergic neuronal loss in a rat model of AAV α-synucleinopathy. J. Neurosci. 29, 3365–3373.

Dinter, E., Saridaki, T., Nippold, M., Plum, S., Diederichs, L., Komnig, D., Fensky, L., May, C., Marcus, K., Voigt, A., Schulz, J.B., Falkenburger, B.H., 2016. Rab7 induces clearance of α-synuclein aggregates. J. Neurochem. 138, 758–774.

Dunn, K.W., Kamocka, M.M., McDonald, J.H., 2011. A practical guide to evaluating colocalization in biological microscopy. Am. J. Physiol. 300 (4), 723–742.

Eapen, V.V., Waterman, D.P., Bernard, A., Schiffmann, N., Sayas, E., Kamber, R., Lemos, B., Memisoglu, G., Ang, J., Mazella, A., Chuartzman, S.G., Loewith, R.J., Schuldiner, M., Denic, V., Klionsky, D.J., Haber, J.E., 2017. A pathway of targeted autophagy is induced by DNA damage in budding yeast. Proc. Natl. Acad. Sci. U. S. A. 114, E1158–E1167.

Elbaz-Alon, Y., Guo, Y., Segev, N., Harel, M., Quinnell, D.E., Geiger, T., Avinoam, O., Li, D., Nunnari, J., 2020. PDZD8 interacts with Protrudin and Rab7 at ER-late endosome membrane contact sites associated with mitochondria. Nat. Commun. 11.

Eriksen, J., Bjørn-Yoshimoto, W.E., Jørgensen, T.N., Newman, A.H., Gether, U., 2010. Postendocytic sorting of constitutively internalized dopamine transporter in cell lines and dopaminergic neurons. J. Biol. Chem. 285, 27289–27301.

Frudd, K., Burgoyne, T., Burgoyne, J.R., 2018. Oxidation of Atg3 and Atg7 mediates inhibition of autophagy. Nat. Commun. 9.
Galati, S., Boni, C., Gerra, M.C., Lazzaretti, M., Buschini, A., 2019. Autophagy: a player in response to oxidative stress and DNA damage. Oxidative Med. Cell. Longev. 2019.
Gao, Y., Wilson, G.R., Stephenson, S.E.M., Bozaoglu, K., Farrer, M.J., Lockhart, P.J., 2018. The emerging role of Rab GTPases in the pathogenesis of Parkinson's disease. Mov. Disord. 33 (2), 196–207.
Goodwin, J., Nath, S., Engelborghs, Y., Pountney, D.L., 2013. Raised calcium and oxidative stress cooperatively promote alpha-synuclein aggregate formation. Neurochem. Int. 62 (5), 703–711.
Guo, J.Y., Karsli-Uzunbas, G., Mathew, R., Aisner, S.C., Kamphorst, J.J., Strohecker, A. M., Chen, G., Price, S., Lu, W., Teng, X., Snyder, E., Santanam, U., DiPaola, R.S., Jacks, T., Rabinowitz, J.D., White, E., 2013. Autophagy suppresses progression of K-ras-induced lung tumors to oncocytomas and maintains lipid homeostasis. Genes Dev. 27, 1447–1461.
Gutierrez, M.G., Munafó, D.B., Berón, W., Colombo, M.I., 2004. Rab7 is required for the normal progression of the autophagic pathway in mammalian cells. J. Cell Sci. 117, 2687–2697.
Horiuchi, H., Lippé, R., McBride, H.M., Rubino, M., Woodman, P., Stenmark, H., Rybin, V., Wilm, M., Ashman, K., Mann, M., Zerial, M., 1997. A novel Rab5 GDP/GTP exchange factor complexed to Rabaptin-5 links nucleotide exchange to effector recruitment and function. Cell 90, 1149–1159.
Hunn, B.H.M., Vingill, S., Threlfell, S., Alegre-Abarrategui, J., Magdelyns, M., Deltheil, T., Bengoa-Vergniory, N., Oliver, P.L., Cioroch, M., Doig, N.M., Bannerman, D.M., Cragg, S.J., Wade-Martins, R., 2019. Impairment of macroautophagy in dopamine neurons has opposing effects on Parkinsonian pathology and behavior. Cell Rep. 29, 920–931 (e7).
Jäger, S., Bucci, C., Tanida, I., Ueno, T., Kominami, E., Saftig, P., Eskelinen, E.L., 2004. Role for Rab7 in maturation of late autophagic vacuoles. J. Cell Sci. 117, 4837–4848.
Jongsma, M.L., Bakker, J., Cabukusta, B., Liv, N., Elsland, D., Fermie, J., Akkermans, J.L., Kuijl, C., Zanden, S.Y., Janssen, L., Hoogzaad, D., Kant, R., Wijdeven, R.H., Klumperman, J., Berlin, I., Neefjes, J., 2020. SKIP HOPS recruits TBC1D15 for a Rab7-to-Arl8b identity switch to control late endosome transport. EMBO J. 39.
Junn, E., Mouradian, M.M., 2002. Human α-synuclein over-expression increases intracellular reactive oxygen species levels and susceptibility to dopamine. Neurosci. Lett. 320, 146–150.
Karpinar, D.P., Balija, M.B.G., Kügler, S., Opazo, F., Rezaei-Ghaleh, N., Wender, N., Kim, H.-Y., Taschenberger, G., Falkenburger, B.H., Heise, H., Kumar, A., Riedel, D., Fichtner, L., Voigt, A., Braus, G.H., Giller, K., Becker, S., Herzig, A., Baldus, M., Jäckle, H., Eimer, S., Schulz, J.B., Griesinger, C., Zweckstetter, M., 2009. Pre-fibrillar alpha-synuclein variants with impaired beta-structure increase neurotoxicity in Parkinson's disease models. EMBO J. 28, 3256–3268.
Kiffin, R., Bandyopadhyay, U., Cuervo, A.M., 2006. Oxidative stress and autophagy. Antioxidants Redox Signal. 8 (1–2), 152–162.
Kjos, I., Borg Distefano, M., Sætre, F., Repnik, U., Holland, P., Jones, A.T., Engedal, N., Simonsen, A., Bakke, O., Progida, C., 2017. Rab7b modulates autophagic flux by interacting with Atg4B. EMBO Rep. 18, 1727–1739.
Klucken, J., Poehler, A.M., Ebrahimi-Fakhari, D., Schneider, J., Nuber, S., Rockenstein, E., Schlötzer-Schrehardt, U., Hyman, B.T., McLean, P.J., Masliah, E., Winkler, J., 2012. Alpha-synuclein aggregation involves a bafilomycin A1-sensitive autophagy pathway. Autophagy 8, 754–766.
Koch, J.C., Bitow, F., Haack, J., D'Hedouville, Z., Zhang, J.-N.N., Tönges, L., Michel, U., Oliveira, L.M.A.A., Jovin, T.M., Liman, J., Tatenhorst, L., Bähr, M., Lingor, P., Hedouville, Z., Zhang, J.-N.N., Tönges, L., Michel, U., Oliveira, L.M.A.A., Jovin, T. M., Liman, J., Tatenhorst, L., Bähr, M., Lingor, P., 2015. Alpha-Synuclein affects neurite morphology, autophagy, vesicle transport and axonal degeneration in CNS neurons. Cell Death Dis. 6, e1811.
Kowsky, S., Pöppelmeyer, C., Kramer, E.R., Falkenburger, B.H., Kruse, A., Klein, R., Schulz, J.B., 2007. RET signaling does not modulate MPTP toxicity but is required for regeneration of dopaminergic axon terminals. Proc. Natl. Acad. Sci. U. S. A. 104, 20049–20054.
Kuchitsu, Y., Fukuda, M., 2018. Revisiting Rab7 functions in mammalian autophagy: Rab7 knockout studies. Cells 7, 215.
Langemeyer, L., Fröhlich, F., Ungermann, C., 2018. Rab GTPase function in endosome and lysosome biogenesis. Trends Cell Biol. 28 (11), 957–970.
Lee, J., Zhu, W.M., Stanic, D., Finkelstein, D.I., Horne, M.H., Henderson, J., Lawrence, A. J., O'Connor, L., Tomas, D., Drago, J., Horne, M.K., 2008. Sprouting of dopamine terminals and altered dopamine release and uptake in Parkinsonian dyskinaesia. Brain 131, 1574–1587.
Martin, L.J., Pan, Y., Price, A.C., Sterling, W., Copeland, N.G., Jenkins, N.A., Price, D.L., Lee, M.K., 2006. Parkinson's disease α-synuclein transgenic mice develop neuronal mitochondrial degeneration and cell death. J. Neurosci. 26, 41–50.
Marwaha, R., Arya, S.B., Jagga, D., Kaur, H., Tuli, A., Sharma, M., 2017. The Rab7 effector PLE KHM1 binds Arl8b to promote cargo traffic to lysosomes. J. Cell Biol. 216, 1051–1070.
Masliah, E., Rockenstein, E., Veinbergs, I., Mallory, M., Hashimoto, M., Takeda, A., Sagara, Y., Sisk, A., Mucke, L., 2000. Dopaminergic loss and inclusion body formation in α-synuclein mice: implications for neurodegenerative disorders. Science (80-.) 287, 1265–1269.
Meneses-Salas, E., García-Melero, A., Kanerva, K., Blanco-Muñoz, P., Morales-Paytuvi, F., Bonjoch, J., Casas, J., Egert, A., Beevi, S.S., Jose, J., Llorente-Cortés, V., Rye, K.A., Heeren, J., Lu, A., Pol, A., Tebar, F., Ikonen, E., Grewal, T., Enrich, C., Rentero, C., 2020. Annexin A6 modulates TBC1D15/Rab7/StARD3 axis to control endosomal cholesterol export in NPC1 cells. Cell. Mol. Life Sci. 77, 2839–2857.
Milanese, C., Cerri, S., Ulusoy, A., Gornati, S.V., Plat, A., Gabriels, S., Blandini, F., Di Monte, D.A., Hoeijmakers, J.H., Mastroberardino, P.G., 2018. Activation of the DNA damage response in vivo in synucleinopathy models of Parkinson's disease. Cell Death Dis. 9.
Minakaki, G., Menges, S., Kittel, A., Emmanouilidou, E., Schaeffner, I., Barkovits, K., Bergmann, A., Rockenstein, E., Adame, A., Marxreiter, F., Mollenhauer, B., Galasko, D., Buzás, E.I., Schlötzer-Schrehardt, U., Marcus, K., Xiang, W., Lie, D.C., Vekrellis, K., Masliah, E., Winkler, J., Klucken, J., 2018. Autophagy inhibition promotes SNCA/alpha-synuclein release and transfer via extracellular vesicles with a hybrid autophagosome-exosome-like phenotype. Autophagy 14, 98–119.
Musgrove, R.E., Helwig, M., Bae, E.J., Aboutalebi, H., Lee, S.J., Ulusoy, A., Di Monte, D. A., 2019. Oxidative stress in vagal neurons promotes parkinsonian pathology and intercellular α-synuclein transfer. J. Clin. Invest. 129, 3738–3753.
Nichols, M.R., St-Pierre, M.K., Wendeln, A.C., Makoni, N.J., Gouwens, L.K., Garrad, E.C., Sohrabi, M., Neher, J.J., Tremblay, M.E., Combs, C.K., 2019. Inflammatory mechanisms in neurodegeneration. J. Neurochem. 149 (5), 562–581.
Oliveira, J.M.A., Chen, S., Almeida, S., Riley, R., Gonçalves, J., Oliveira, C.R., Hayden, M. R., Nicholls, D.G., Ellerby, L.M., Rego, A.C., 2006. Mitochondrial-dependent Ca2+ handling in Huntington's disease striatal cells: effect of histone deacetylase inhibitors. J. Neurosci. 26, 11174–11186.
Paiva, I., Pinho, R., Pavlou, M.A., Hennion, M., Wales, P., Schütz, A.L., Rajput, A., Szego, É.M., Kerimoglu, C., Gerhardt, E., Rego, A.C., Fischer, A., Bonn, S., Outeiro, T. F., 2017. Sodium butyrate rescues dopaminergic cells from alpha-synuclein-induced transcriptional deregulation and DNA damage. Hum. Mol. Genet. 26, 2231–2246.
Panier, S., Boulton, S.J., 2014. Double-strand break repair: 53BP1 comes into focus. Nat. Rev. Mol. Cell Biol. 15 (1), 7–18.
Park, J.W., Vahidi, B., Taylor, A.M., Rhee, S.W., Jeon, N.L., 2006. Microfluidic culture platform for neuroscience research. Nat. Protoc. 1, 2128–2136.
Pekny, M., Wilhelmsson, U., Pekna, M., 2014. The dual role of astrocyte activation and reactive gliosis. Neurosci. Lett. 565, 30–38.
Saridaki, T., Nippold, M., Dinter, E., Roos, A., Diederichs, L., Fensky, L., Schulz, J.B., Falkenburger, B.H., 2018. FYCO1 mediates clearance of α-synuclein aggregates through a Rab7-dependent mechanism. J. Neurochem. 146, 474–492.
Schaser, A.J., Osterberg, V.R., Dent, S.E., Stackhouse, T.L., Wakeham, C.M., Boutros, S. W., Weston, L.J., Owen, N., Weissman, T.A., Luna, E., Raber, J., Luk, K.C., McCullough, A.K., Woltjer, R.L., Unni, V.K., 2019. Alpha-synuclein is a DNA binding protein that modulates DNA repair with implications for Lewy body disorders. Sci. Rep. 9, 1–19.
Schmitz, C., Hof, P.R., 2005. Design-based stereology in neuroscience. Neuroscience 130 (4), 813–831.
Scudamore, O., Ciossek, T., 2018. Increased oxidative stress exacerbates α-synuclein aggregation in vivo. J. Neuropathol. Exp. Neurol. 77, 443–453.
Sidransky, E., Nalls, M.A., Aasly, J.O., Aharon-Peretz, J., Annesi, G., Barbosa, E.R., Bar-Shira, A., Berg, D., Bras, J., Brice, A., Chen, C.-M., Clark, L.N., Condroyer, C., De Marco, E.V., Dürr, A., Eblan, M.J., Fahn, S., Farrer, M.J., Fung, H.-C., Gan-Or, Z., Gasser, T., Gershoni-Baruch, R., Giladi, N., Griffith, A., Gurevich, T., Januario, C., Kropp, P., Lang, A.E., Lee-Chen, G.-J., Lesage, S., Marder, K., Mata, I.F., Mirelman, A., Mitsui, J., Mizuta, I., Nicoletti, G., Oliveira, C., Ottman, R., Orr-Urtreger, A., Pereira, L.V., Quattrone, A., Rogaeva, E., Rolfs, A., Rosenbaum, H., Rozenberg, R., Samii, A., Samaddar, T., Schulte, C., Sharma, M., Singleton, A., Spitz, M., Tan, E.-K., Tayebi, N., Toda, T., Troiano, A.R., Tsuji, S., Wittstock, M., Wolfsberg, T.G., Wu, Y.-R., Zabetian, C.P., Zhao, Y., Ziegler, S.G., 2009. Multicenter analysis of glucocerebrosidase mutations in Parkinson's disease. N. Engl. J. Med. 361, 1651–1661.
Spinosa, M.R., Progida, C., De Luca, A., Colucci, A.M.R., Alifano, P., Bucci, C., 2008. Functional characterization of Rab7 mutant proteins associated with Charcot-Marie-Tooth type 2B disease. J. Neurosci. 28, 1640–1648.
Suzuki, G., Imura, S., Hosokawa, M., Katsumata, R., Nonaka, T., Hisanaga, S.I., Saeki, Y., Hasegawa, M., 2020. α-Synuclein strains that cause distinct pathologies differentially inhibit proteasome. Elife 9, 1–21.
Szegő, É.M., Gerhardt, E., Kermer, P., Schulz, J.B., 2012. A30P α-synuclein impairs dopaminergic fiber regeneration and interacts with L-DOPA replacement in MPTP-treated mice. Neurobiol. Dis. 45, 591–600.
Szegő, É.M., Gerhardt, E., Outeiro, T.F., 2017. Sirtuin 2 enhances dopaminergic differentiation via the AKT/GSK-3β/β-catenin pathway. Neurobiol. Aging 56, 7–16.
Szegő, É.M., Dominguez-Meijide, A., Gerhardt, E., König, A., Koss, D.J., Li, W., Pinho, R., Fahlbusch, C., Johnson, M., Santos, P., Villar-Piqué, A., Thom, T., Rizzoli, S., Schmitz, M., Li, J., Zerr, I., Attems, J., Jahn, O., Outeiro, T.F., 2019. Cytosolic trapping of a mitochondrial heat shock protein is an early pathological event in synucleinopathies. Cell Rep. 28, 65–77 (e6).
Szegő, É.M., Boß, F., Komnig, D., Gärtner, C., Höfs, L., Shaykhalishahi, H., Woerdehoff, M., Saridaki, T., Schulz, J.B., Hoyer, W., Falkenburger, B.H., 2021. A β-wrapin targeting the N-terminus of α-synuclein monomers reduces fibril-induced aggregation in neurons. Front. Neurosci. 15, 751.
Tomas, D., Stanic, D., Chua, H.K., White, K., Boon, W.C., Horne, M., 2016. Restoration of the dopamine transporter through cell therapy improves dyskinesia in a rat model of Parkinson's disease. PLoS One 11, e0153424.
van den Boomen, D.J.H., Sienkiewicz, A., Berlin, I., Jongsma, M.L.M., van Elsland, D.M., Luzio, J.P., Neefjes, J.J.C., Lehner, P.J., 2020. A trimeric Rab7 GEF controls NPC1-dependent lysosomal cholesterol export. Nat. Commun. 11.
Van Der Perren, A., Toelen, J., Carlon, M., Van Den Haute, C., Coun, F., Heeman, B., Reumers, V., Vandenberghe, L.H., Wilson, J.M., Debyser, Z., Baekelandt, V., 2011. Efficient and stable transduction of dopaminergic neurons in rat substantia nigra by rAAV 2/1, 2/2, 2/5, 2/6.2, 2/7, 2/8 and 2/9. Gene Ther. 18, 517–527.
Van der Perren, A., Toelen, J., Casteels, C., Macchi, F., Van Rompuy, A.S., Sarre, S., Casadei, N., Nuber, S., Himmelreich, U., Osorio Garcia, M.I., Michotte, Y., D'Hooge, R., Bormans, G., Van Laere, K., Gijsbers, R., Van den Haute, C., Debyser, Z., Baekelandt, V., 2015. Longitudinal follow-up and characterization of a robust rat

model for Parkinson's disease based on overexpression of alpha-synuclein with adeno-associated viral vectors. Neurobiol. Aging 36, 1543–1558.
Van der Perren, A., Casteels, C., Van Laere, K., Gijsbers, R., Van den Haute, C., Baekelandt, V., 2016. Development of an alpha-synuclein based rat model for Parkinson's disease via stereotactic injection of a recombinant adeno-associated viral vector. J. Vis. Exp. 2016, 53670.
Verstraeten, A., Theuns, J., Van Broeckhoven, C., 2015. Progress in unraveling the genetic etiology of Parkinson disease in a genomic era. Trends Genet. 31 (3), 140–149.
Volpicelli-Daley, L.A., Luk, K.C., Lee, V.M.-Y., 2014. Addition of exogenous α-synuclein preformed fibrils to primary neuronal cultures to seed recruitment of endogenous α-synuclein to Lewy body and Lewy neurite-like aggregates. Nat. Protoc. 9 (9), 135–146.
Wang, Z., Miao, G., Xue, X., Guo, X., Yuan, C., Wang, Zhaoyu, Zhang, G., Chen, Y., Feng, D., Hu, J., Zhang, H., 2016a. The Vici syndrome protein EPG5 is a Rab7 effector that determines the fusion specificity of autophagosomes with late endosomes/lysosomes. Mol. Cell 63, 781–795.
Wang, D., Yu, T., Liu, Y., Yan, J., Guo, Y., Jing, Y., Yang, X., Song, Y., Tian, Y., 2016b. DNA damage preceding dopamine neuron degeneration in A53T human α-synuclein transgenic mice. Biochem. Biophys. Res. Commun. 481, 104–110.
Wen, H., Zhan, L., Chen, S., Long, L., Xu, E., 2017. Rab7 may be a novel therapeutic target for neurologic diseases as a key regulator in autophagy. J. Neurosci. Res. 95, 1993–2004.
Winslow, A.R., Rubinsztein, D.C., 2011. The Parkinson disease protein α-synuclein inhibits autophagy. Autophagy 7 (4), 429–431.
Wu, S., Fagan, R.R., Uttamapinant, C., Lifshitz, L.M., Fogarty, K.E., Ting, A.Y., Melikian, H.E., 2017. The dopamine transporter recycles via a retromer-dependent postendocytic mechanism: tracking studies using a novel fluorophore-coupling approach. J. Neurosci. 37, 9438–9452.
Xiao, W., Yeerken, D., Li, J., Li, Z., Jiang, L., Li, D., Fu, M., Ma, L., Song, Y., Zhang, W., Zhan, Q., 2021. Nlp promotes autophagy through facilitating the interaction of Rab7 and FYCO1. Signal Transduct. Target. Ther. 6.
Zhan, L., Chen, S., Li, K., Liang, D., Zhu, X., Liu, L., Lu, Z., Sun, W., Xu, E., 2017. Autophagosome maturation mediated by Rab7 contributes to neuroprotection of hypoxic preconditioning against global cerebral ischemia in rats. Cell Death Dis. 8, e2949.
Zhang, M., Chen, L., Wang, S., Wang, T., 2009. Rab7: roles in membrane trafficking and disease. Biosci. Rep. 29 (3), 193–209.
Zhao, Y.G., Zhang, H., 2019. Autophagosome maturation: an epic journey from the ER to lysosomes. J. Cell Biol. 218 (3), 757–770.